



Research Article

Galaxy evolution through infrared and submillimetre spectroscopy: Measuring star formation and black hole accretion with JWST and ALMA

Sabrina Mordini^{1,2} , Luigi Spinoglio² and Juan Antonio Fernández-Ontiveros^{2,3} 

¹Dipartimento di Fisica, Università di Roma La Sapienza, P.le A. Moro 2, I-00185 Roma, Italy, ²Istituto di Astrofisica e Planetologia Spaziali (INAF-IAPS), Via Fosso del Cavaliere 100, I-00133 Roma, Italy and ³Centro de Estudios de Física del Cosmos de Aragón (CEFCA), Plaza San Juan 1, E-44001, Teruel, Spain

Abstract

Rest-frame mid- to far-infrared (IR) spectroscopy is a powerful tool to study how galaxies formed and evolved, because a major part of their evolution occurs in heavily dust enshrouded environments, especially at the so-called Cosmic Noon ($1 < z < 3$). Using the calibrations of IR lines and features, recently updated with *Herschel* and *Spitzer* spectroscopy, we predict their expected fluxes with the aim to measure the Star Formation (SF) and the Black Hole Accretion (BHA) rates in intermediate to high redshift galaxies. On the one hand, the recent launch of the *James Webb Space Telescope* (JWST) offers new mid-IR spectroscopic capabilities that will enable for the first time a detailed investigation of both the SF and the BHA obscured processes as a function of cosmic time. We make an assessment of the spectral lines and features that can be detected by JWST-MIRI in galaxies and active galactic nuclei up to redshift $z \sim 3$. The fine structure lines of [MgIV]4.49 μm and [ArVI]4.53 μm can be used as BHA rate tracers for the $1 \lesssim z \lesssim 3$ range, and we propose the [NeVI]7.65 μm line as the best tracer for $z \lesssim 1.5$. The [ArII]6.98 μm and [ArIII]8.99 μm lines can be used to measure the SF rate at $z \lesssim 3$ and $z \lesssim 2$, respectively, while the stronger [NeII]12.8 μm line exits the JWST-MIRI spectral range above $z \gtrsim 1.2$. At higher redshifts, the PAH features at 6.2 and 7.7 μm can be observed at $z \lesssim 3$ and $z \lesssim 2.7$, respectively. On the other hand, rest-frame far-IR spectroscopic observations of high redshift galaxies ($z \gtrsim 3$) have been collected with the Atacama Large Millimeter Array (ALMA) in the last few years. The observability of far-IR lines from ALMA depends on the observed frequency, due to the significant decrease of the atmospheric transmission at the highest frequencies ($\gtrsim 420$ Hz). The [CII]158 μm line is a reliable tracer of the SF rate and can in most cases ($0.9 \lesssim z \lesssim 2$ and $2 \lesssim z \lesssim 9$) be observed. Additionally, we propose the use of the combination of [OIII]88 μm and [OI]145 μm lines as an alternative SF rate tracer, that can be detected above $z \gtrsim 3$. Overall, we emphasize the importance of using multi-feature analysis to measure both BHA and SFR, since individual tracers can be strongly dependent on the local ISM conditions and vary from source to source. However, we conclude that the peak of the obscured SF and BHA activities at Cosmic Noon falls outside the wavelength coverage of facilities currently operating or under development. A new IR space telescope covering the full IR spectral range from about 10 to 300 μm and actively cooled to achieve high sensitivity, will be needed.

Keywords: galaxies: active – galaxies: evolution – galaxies: star formation – infrared: galaxies – techniques: spectroscopic – telescopes

(Received 4 November 2021; revised 28 February 2022; accepted 7 March 2022)

1. Introduction

The formation and evolution of galaxies is one of the main fields of study in modern astrophysics, nevertheless it has serious limitations due to our lack of knowledge concerning the main processes that drive the evolution. These are the two sources of energy in galaxies, i.e. star formation with the subsequent stellar evolution, and the accretion onto supermassive black holes in active galactic nuclei (AGN). The bulk of activity, however, takes place in heavily dust obscured environments during the so-called *Cosmic Noon* ($z \sim 1 - 3$), where almost 90% of optical and UV radiation is absorbed by dust and re-emitted at longer wavelengths (Madau & Dickinson 2014; Heckman & Best 2014), then followed by a steep decline toward the present epoch. Thus, to fully characterize the

various phenomena driving galaxy evolution and their interplay is paramount to explore galaxies throughout their dust obscured phase (e.g. Spinoglio et al. 2017, 2021a).

The mid- to far-infrared (IR) spectral range is populated by a wealth of lines and features which offer an ideal tool to probe the dust hidden regions where the bulk of activity in galaxies takes place (e.g. Spinoglio & Malkan 1992; Armus et al. 2007). The various fine-structure lines in this range cover a wide range of physical parameters such as density, ionization and excitation, and can be used to discriminate between the different conditions of the interstellar medium and the processes taking place there. Most of these lines, however, can be observed only from space IR telescopes, while only a limited number of transitions are detectable by ground-based facilities. In particular, AGN activity can be traced by high-ionization lines, while low to intermediate ionization fine-structure lines are good tracers of star formation processes.

The *James Webb Space Telescope* (JWST, Gardner et al. 2006), successfully launched in December 2021, will observe the Universe

Corresponding author: Sabrina Mordini, email: sabrina.mordini@inaf.it

Cite this article: Mordini S, Spinoglio L and Fernández-Ontiveros JA. (2022) Galaxy evolution through infrared and submillimetre spectroscopy: Measuring star formation and black hole accretion with JWST and ALMA. *Publications of the Astronomical Society of Australia* 39, e012, 1–16. <https://doi.org/10.1017/pasa.2022.10>

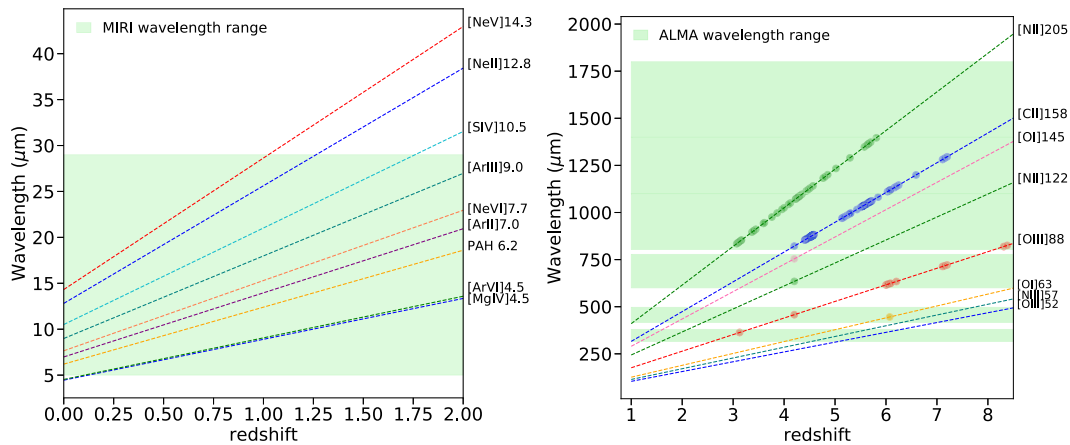


Figure 1. *Left:* observability of key mid-IR (dashed lines) lines as a function of redshift. The shaded area shows the redshift interval covered by the *JWST*-MIRI instrument spectral range. *Right:* observability of key far-IR (dashed lines) lines compared to the ALMA bands (shaded area) in the 1-8 redshift interval. Dots represent current detection for each line. Figure adapted from Mordini, Spinoglio, & Fernández-Ontiveros (2021).

in the near- to mid-IR range. In particular, the Mid-Infrared Instrument (MIRI, Rieke et al. 2015; Wright et al. 2015) will be able to obtain imaging and spectra with unprecedented sensitivity in the 4.9–28.9 μm range. In the near future, the extremely large ground-based telescopes, currently under construction, will have dedicated instruments to obtain spectroscopic observations in the *N* band atmospheric window at 8–13 μm , and thus will be able to measure the [SIV]10.5 μm and [NeII]12.8 μm fine-structure lines, and the 11.3 μm PAH band in local galaxies. First light from the ESO Extremely Large telescope (E-ELT; Gilmozzi & Spyromilio 2007) is expected by the end of 2025, with the Mid-infrared ELT Imager and Spectrograph (METIS; Brandl et al. 2021) covering the *N* band with both imaging and low resolution spectroscopy; the Thirty Meter Telescope (TMT; Schöck et al. 2009) is expected to be ready for science by the end of 2027, and the Giant Magellan Telescope (GMT; Johns et al. 2012) will be operational in 2029.

At the present time, only the *Stratospheric Observatory For Infrared Astronomy* (SOFIA; Gehrz et al. 2009), observing from the high atmosphere, can cover the full mid- to far-IR spectral range and detect line emission from the brightest galaxies in the local Universe, although with limitations due to atmospheric absorption and emission. An example of successful SOFIA spectroscopic observations of the [OIII]52 μm and [NIII]57 μm far-IR lines in local galaxies, aimed at the measurement of chemical abundances, can be found in Spinoglio et al. (2021b). At much longer wavelengths, in the submillimeter domain, the Atacama Large Millimeter Array (ALMA; Wootten & Thompson 2009) can observe within the submillimeter atmospheric bands centered at ~ 0.35 and 0.45 mm, and the 0.6–3.6 mm range. However, the shorter wavelength bands are accessible only when the precipitable water vapour content of the atmosphere is low enough ($\text{PWV} \lesssim 0.5$ mm) to obtain a peak transmission of about 50%.

In this article, we assess the detection of star formation and BHA tracers, using the *JWST*-MIRI spectrometer and the ALMA telescope, by computing the predicted fluxes of key lines as a function of redshift, comparing them with the sensitivity of the two instruments. The work is organized as follows. Sections 1.1 and 1.2 briefly describe the capabilities of the *JWST*-MIRI instrument and the ALMA observatory, respectively, for studying galaxy

evolution. Section 2 describes the approach used to derive the predicted line fluxes. Section 3 reports our results, in particular the predictions for *JWST* are analysed in Section 3.1, while those for ALMA are in Section 3.2. In Section 4, we provide the prescriptions to measure the SFR and the BHAR with *JWST* and ALMA. These results are discussed in Section 5, and the main conclusions of this work are presented in Section 6.

1.1. The Cosmic Noon as seen by *JWST* in the mid-IR

The *JWST*-MIRI instrument can perform spectroscopic imaging observations in the 4.9–28.9 μm range through four integral field units. The left panel in Figure 1 shows the instrument spectral range and the maximum redshift at which the main key lines and features in the mid-IR range can be observed. The *JWST*-MIRI cut-off wavelength of ~ 29 μm significantly limits the possibility of probing accretion phenomena using the brightest high-excitation lines, which are beyond reach at $z > 1$, missing about half of the cosmic accretion history. The best BHAR tracers in the mid-IR are [Ne V]14.3, 24.3 μm and [O IV]25.9 μm (see, e.g. Sturm et al. 2002; Meléndez et al. 2008; Tommasin et al. 2008; Tommasin et al. 2010). The [Ne V]24.3 μm and [OIV]25.9 μm lines are not shown in the left panel of Figure 1 due to the limited range available: the former can be observed up to redshift $z \simeq 0.15$, whereas the latter escapes above $z \simeq 0.1$. The [Ne V]14.3 μm line can be observed by *JWST*-MIRI up to redshift $z \simeq 1$.

Alternative BHAR tracers that could be exploited by *JWST*-MIRI beyond $z \sim 1$ have been recently proposed by Satyapal et al. (2021). These authors use photo-ionization simulations to investigate possible spectral diagnostics that separate the AGN and star formation contribution in galaxies using MIRI and NIRSpc (Near Infrared Spectrograph; Bagnasco et al. 2007; Birkmann et al. 2016). In particular, they propose [MgIV]4.49 μm , [ArVI]4.53 μm and [NeVI]7.65 μm as the best tracers to identify heavily obscured AGN with moderate luminosities up to $z \sim 3$. These lines, however, have not been extensively observed so far, and thus the predictions are completely based on photo-ionization models.

On the other hand, star formation can be traced up to $z \sim 2$ using PAH features, nevertheless the behaviour of these features

in high redshift galaxies is not yet well understood. These aromatic compounds could in fact be destroyed by strong radiation fields and/or be less efficiently formed in low metallicity environments, (e.g. Engelbracht et al. 2008; Cormier et al. 2015; Galliano et al. 2021). While alternative SFR tracers based in optical lines (e.g. Álvarez-Márquez et al. 2019) or continuum band fluxes (e.g. Senarath et al. 2018) could be used, the potential of mid-IR spectroscopic tracers is a far more relevant for the study of dust-obscured galaxies (Ho & Keto 2007).

1.2. Galaxy evolution with ALMA beyond the Cosmic Noon

While JWST will allow us to probe galaxies at redshift below $z \lesssim 3$ using mid-IR lines, the ALMA telescope has already studied a number of galaxies at $z \gtrsim 3$. In particular, the SFR can be traced using far-IR lines, i.e. [OIII]88 μm and [CII]158 μm up to $z \simeq 8$, as shown in the right panel of Figure 1. An analogous figure can be found in (Carilli & Walter 2013, see their Figure 1), where the CO transitions and other key tracers of the ISM are shown as a function of redshift versus frequency in terms of the observability by ALMA and JVLA (Karl J. Jansky Very Large Array, Perley et al. 2011). As can be seen in the right panel of Figure 1, the [OIII]88 μm , [CII]158 μm and [NII]205 μm lines have been detected over an extended redshift interval, from $z \sim 3 - 4$ to $z \sim 6 - 8$, while the shorter wavelength lines such as [OI]63 μm show very few observations. No detections have been reported so far for the [OIII]52 μm and [NIII]57 μm lines with ALMA. This is due to the technical difficulty of observing at the highest frequencies, where the atmospheric absorption limits the available observing time to a $\sim 10\%$ of the total. While ALMA cannot detect these far-IR lines in galaxies at the peak of their activity ($1 \lesssim z \lesssim 3$), it allows us to probe galaxies at earlier epochs, thus shedding light on the processes that led to the Cosmic Noon. Observations of the rest-frame far-IR continuum in galaxies after the reionization epoch suggest that large amounts of dust were already present in these objects (e.g. Laporte et al. 2017), and therefore IR tracers will be required in order to probe the ISM and understand the physical processes taking place in those galaxies.

2. Methods

We assess how the JWST-MIRI and ALMA instruments can measure the star formation rate (SFR) and the black hole accretion rate (BHAR) covering, respectively, the $z \lesssim 3$ and $z \gtrsim 3$ redshift intervals. The predictions for JWST-MIRI have been derived using the CLOUDY (Ferland et al. 2017) photo-ionization models computed by Fernández-Ontiveros et al. (2016), using the BPASS v2.2 stellar population synthetic library (Stanway & Eldridge 2018) for the case of the star forming models. We consider, in particular, three classes of objects, as presented in Mordini et al. (2021): (i) AGN, (ii) star forming galaxies (SFG), and (iii) low metallicity galaxies (LMG) covering the $\sim 7 \leq 12 + \log(\text{O}/\text{H}) \leq 8.5$ metallicity range (Madden et al. 2013; Cormier et al. 2015). This is motivated by the detection of massive galaxies ($\sim 10^{10} M_{\odot}$) in optical surveys with sub-solar metallicities during the Cosmic Noon, which may experience a fast chemical evolution above $z \sim 2$ (Maiolino et al. 2008; Mannucci et al. 2009; Troncoso et al. 2014; Onodera et al. 2016). These changes are expected to have an impact on the ISM structure of high- z galaxies, favouring stronger radiation fields (e.g. Steidel et al. 2016; Kashino et al. 2019; Sanders et al. 2020) and a more porous ISM similar to that observed in dwarf galaxies (Cormier et al. 2019).

Table 1. The fine-structure lines in the mid- to far-IR range used in this work. For each line, the columns give: central wavelength, frequency, ionization potential, excitation temperature and critical density. Critical densities and excitation temperatures are from: Launay & Roueff (1977), Tielens & Hollenbach (1985), Greenhouse et al. (1993), Sturm et al. (2002), Cormier et al. (2012), Goldsmith et al. (2012), Farrah et al. (2013), Satyapal et al. (2021). Adapted from Mordini et al. (2021).

Line	λ (μm)	ν (GHz)	I.P. (eV)	E (K)	n_{cr} (cm^{-3})
[MgIV]	4.49	66811.78	80	-	1.258×10^7
[ArVI]	4.53	66208.58	75	-	7.621×10^5
[ArII]	6.98	42929.48	16	-	4.192×10^5
[NeVI]	7.65	39188.56	126.21	1888	2.5×10^5
[ArIII]	8.99	33351.11	28	-	3.491×10^5
[SiV]	10.51	28524.50	34.79	1369	5.39×10^4
[NeII]	12.81	23403.00	21.56	1123	7.00×10^5
[NeV]	14.32	20935.23	97.12	1892	3×10^4
[OI]	63.18	4744.77	-	228	4.7×10^5 a
[OIII]	88.36	3393.01	35.12	163	510
[NII]	121.90	2459.38	14.53	118	310
[OI]	145.52	2060.07	-	98	9.5×10^4 a
[CII]	157.74	1900.54	11.26	91	$20, [2.2a, 4.4b] \times 10^3$
[NII]	205.3	1460.27	14.53	70	48

^aCritical density for collisions with hydrogen atoms.

^bCritical density for collisions with H_2 molecules.

We have explored the well known problem of the relative weakness of the narrow lines intensities in Seyfert galaxies and quasars at increasing bolometric luminosity, which has been observed in optical forbidden lines (e.g., Stern & Laor 2012). We have tested this hypothesis on a sample of bright PG quasars with [NeV]14.3 μm and [OIV]25.9 μm measurements from Veilleux et al. (2009). For these high-excitation lines, the depression of the line intensities is noticeable for total IR luminosities above $10^{45} \sim \text{erg s}^{-1}$. This value is larger than the luminosity range covered by the AGN sample used to derive the IR fine structure line calibrations ($10^{42} < L_{IR} < 10^{45} \sim \text{erg s}^{-1}$; Mordini et al. 2021), thus we conclude that this effect is not biasing our results. It follows, however, that our conclusions are limited to AGN with total luminosities below this threshold, while for brighter objects the predicted accretion luminosities and the accretion rates could be underestimated.

To measure the BHAR, we consider the [MgIV] 4.49 μm , [ArVI] 4.53 μm (see, e.g., Satyapal et al. 2021) and the [NeVI] 7.65 μm line. We need to caution the reader about the use of the [NeVI]7.65 μm line, because its detections by the Infrared Space Observatory (ISO; Sturm et al. 2002), on which is based the calibration (Mordini et al. 2021) are scarce and have only been obtained for the brightest sources, and therefore this calibration is uncertain. The properties of these lines are summarized in Table 1.

For the BHAR tracers, we use the template of an AGN of total IR luminosity of $L_{IR} = 10^{12} L_{\odot}$, to represent the bulk of the population at redshift $z \sim 2$. We use four different photo-ionization models to derive the line intensities, with two values of the ionization parameter: $\log U = -1.5$ and $\log U = -2.5$, and two values of the hydrogen density: $\log(n_H/\text{cm}^{-3}) = 2$ and $\log(n_H/\text{cm}^{-3}) = 4$. The calibration of the line luminosities, against the total IR luminosities, has been derived using the ratios of the high-excitation

Table 2. Line ratios derived from CLOUDY simulations by Fernández-Ontiveros et al. (2016) for AGN, SFG and LMG: $\log(U)$ indicates the logarithm of the ionization parameter, while $\log(n_H)$ indicates the logarithm of the hydrogen density.

AGN	$\log U$	-1.5	-1.5	-2.5	-2.5
	$\log(n_H/\text{cm}^{-3})$	2	4	2	4
	[MgIV]4.49/[NeV]14.3	0.09	0.11	0.72	1.00
	[ArVI]4.53/[NeV]14.3	0.10	0.14	0.03	0.04
	[NeVI]7.68/[NeV]14.3	0.58	0.78	0.04	0.06
SFG	$\log U$	-2.5	-2.5	-3.5	-3.5
	$\log(n_H/\text{cm}^{-3})$	1	3	1	3
	[ArII]6.98/[NeII]12.8	0.05	0.06	0.12	0.12
	[ArIII]8.99/[NeII]12.8	0.66	0.68	0.32	0.32
	$\frac{[\text{ArII}]6.98 + [\text{ArIII}]8.99}{[\text{NeII}]12.8 + [\text{NeIII}]15.6}$	0.30	0.30	0.38	0.38
LMG	$\log U$	-2	-2	-3	-3
	$\log(n_H/\text{cm}^{-3})$	1	3	1	3
	[ArII]6.98/[NeII]12.8	0.12	0.12	0.12	0.11
	[ArIII]8.99/[NeII]12.8	8.31	8.29	1.41	1.40
	$\frac{[\text{ArII}]6.98 + [\text{ArIII}]8.99}{[\text{NeII}]12.8 + [\text{NeIII}]15.6}$	0.19	0.18	0.27	0.27

Table 3. Correlations of the fine-structure line luminosities with the total IR luminosities ($\log L_{\text{line}} = a \log L_{\text{IR}} + b$), derived from the line ratios reported in Table 2. For AGN: $\log U = -2.5$ and $\log(n_H/\text{cm}^{-3}) = 2$; for SFG: $\log U = -3.5$ and $\log(n_H/\text{cm}^{-3}) = 3$ and for LMG: $\log U = -2$ and $\log(n_H/\text{cm}^{-3}) = 1$.

Line	AGN		SFG		LMG	
	a	b	a	b	a	b
[MgIV]4.49	1.32	-5.15	-	-	-	-
[ArVI]4.53	1.32	-6.53	-	-	-	-
[NeVI]7.65	1.32	-6.41	-	-	-	-
[ArII]6.98	-	-	1.04	-4.4	1.37	-5.28
[ArIII]8.99	-	-	1.04	-3.97	1.37	-3.44

magnesium, argon and neon lines relative to the [NeV]14.3 μm line in the photo-ionization models, and the calibration of the [NeV]14.3 μm line from Mordini et al. (2021).

Table 1 gives the key properties of the lines used in this work. Table 2 reports the line ratios used to derive the line intensities for the [MgIV]4.49 μm , [ArVI]4.53 μm , [ArII]6.98 μm , [NeVI]7.65 μm and [ArIII]8.99 μm lines, given the different combinations of ionization parameter and hydrogen densities. Table 3 reports the calibrations computed from the photo-ionization models scaled to the [NeII]12.8 μm and [NeV]14.3 μm lines (see Section 3.1), while the calibrations of the different lines and features in the mid- to far-IR range can be found in Table D.1 in Mordini et al. (2021).

The line ratios derived from the [NeVI] and [MgIV] detections reported in Sturm et al. (2002) are all consistent with AGN characterized by a ionization parameter of $\log U = -1.5$ and hydrogen density of $\log(n_H/\text{cm}^{-3}) = 4$ (see Table 2), or higher, with line ratios of $[\text{NeVI}]/[\text{NeV}] \sim 0.67\text{--}1.4$ and $[\text{MgIV}]/[\text{NeV}] \sim 0.06$. The low number of detections (8 for the [NeVI] line and 3 for the [MgIV] line) suggests that while the [NeVI] line is more easily observable in AGN whose ISM is characterized by a high ionization potential, the average AGN is relatively weaker. For this reason, while the [MgIV] line can give an accurate measure of the

BHAR in average AGN, a comprehensive measure of AGN activity can be achieved using a combination of [MgIV] and [ArVI] or [NeVI] lines, in order to include also powerful AGN.

As SFR tracers, we take into account the [ArII]6.98 μm and [ArIII]8.99 μm lines. We consider both SFG and LMG, deriving, in both cases, the line intensities dependent on the calibration of the [NeII]12.8 μm line (Mordini et al. 2021) considering, for the SFG, photo-ionization models with an ionization parameter of $\log U = -2.5$ and $\log U = -3.5$, and a hydrogen density of $\log(n_H/\text{cm}^{-3}) = 1$ and $\log(n_H/\text{cm}^{-3}) = 3$, for a total of four different cases. For the LMG, we consider an ionization parameter of $\log U = -2$ and $\log U = -3$, and hydrogen densities of $\log(n_H/\text{cm}^{-3}) = 1$ and $\log(n_H/\text{cm}^{-3}) = 3$. In both cases, we assume a total IR luminosity of the galaxy of $L_{\text{IR}} = 10^{12} L_{\odot}$.

The predictions for the ALMA telescope were derived from the line calibrations described in Mordini et al. (2021). While the spectral range covered by ALMA has no unambiguous high ionization line that can be used to trace the BHAR, we explore what lines, or combination of them, can be used to trace the SFR. Following Mordini et al. (2021), we consider the [CII]158 μm line and the sum of two oxygen lines, either the [OI]63 μm and [OIII]88 μm , or the [OI]145 μm and [OIII]88 μm .

3. Results

3.1. Predictions for JWST

In this section, we predict the intensities of the mid-IR lines and features in the 5–9 μm rest-frame range, as derived from CLOUDY models, and compare them with the JWST-MIRI sensitivity, to verify if these lines, used as tracers for SFR and BHAR, can be observed in galaxies and AGN at redshifts $z > 1$. Table 3 reports the derived correlations of the lines used in this work for the most common values of ionization potential ($\log U$) and gas density [$\log(n_H/\text{cm}^{-3})$] for each type of object. For the AGN lines, we use the calibration of the [NeV]14.3 μm line, while for SFG and LMG we use the [NeII]12.8 μm line. Since these correlations are derived from CLOUDY simulations, we do not report the error on the coefficients. Figure 2 shows the sensitivity of JWST-MIRI, highlighting the wavelengths at which the various fine-structure lines and PAH spectral features can be observed in a galaxy at redshift $z = 1$. In the $\sim 5\text{--}16 \mu\text{m}$ observed spectral range, the MIRI sensitivity is below $\sim 2 \times 10^{-20} \text{ W m}^{-2}$ for a 1 h, 5σ observation, while in the $\sim 16\text{--}29 \mu\text{m}$ observed spectral range the sensitivity is increasingly worse, going from $\sim 6 \times 10^{-20} \text{ W m}^{-2}$ at $\sim 16 \mu\text{m}$ to $\sim 10^{-18} \text{ W m}^{-2}$ at $\sim 29 \mu\text{m}$. This makes observing the [SIV]10.5 μm , [NeII]12.8 μm and [NeV]14.3 μm lines at redshift $z = 1$ a challenging task, and rises the need to find and analyze other tracers.

In the 5–16 μm observed spectral range, AGN tracers are the [MgIV]4.49 μm , [ArVI]4.53 μm and [NeVI]7.65 μm lines, while the [ArII]6.98 μm and the [ArIII]8.99 μm lines are tracers for star formation activity, together with the PAH feature at 6.2 μm . Given their relatively short wavelength, these lines can be used to probe the highly obscured galaxies at the Cosmic Noon ($1 \lesssim z \lesssim 3$). While lines in the mid- to far-IR range do not typically suffer from significant dust extinction, the [MgIV] and [ArVI] lines, at wavelengths of $\lambda \sim 4.5$, can be affected by the presence of heavy dust obscuration. In particular, an optical extinction of $A_V \sim 10$ mag would absorb about $\sim 30\%$ of the radiation at 4.5 μm , following

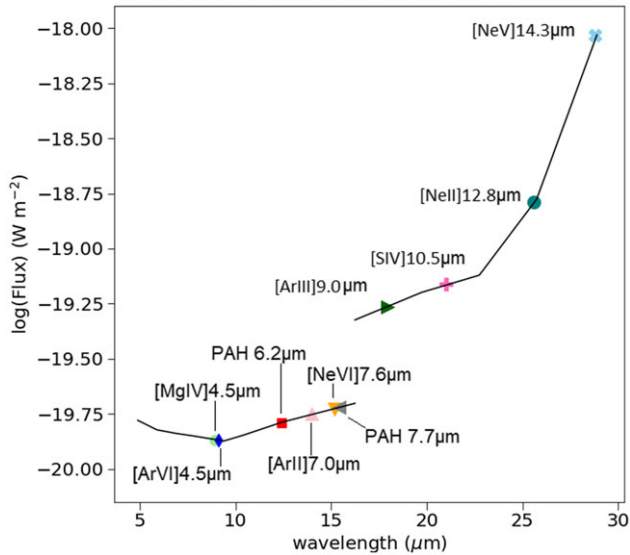


Figure 2. Sensitivity of the JWST-MIRI instrument at different wavelengths, for a 1 h, 5σ observation. The symbols show the position, in the MIRI wavelength range, at which the different lines are observed in a galaxy at redshift $z = 1$. From left to right, the considered lines and feature, at their rest frame wavelength, are: [MgIV] 4.49 μm , [ArVI] 4.53 μm , PAH feature at 6.2 μm , [ArII] 6.98 μm , [NeVI] 7.65 μm , PAH feature at 7.7 μm , [ArIII] 8.99 μm , [SIV] 10.5 μm , [NeII] 12.8 μm and [NeV] 14.3 μm .

the extinction curve of Cardelli et al. (1989). This value increases to $\sim 80\%$ for the very high optical extinction of $A_V \sim 50$ mag.

Figure 3 shows the predicted fluxes, as a function of redshift, compared to the MIRI sensitivity for the [NeV] 14.3 μm (panel a), [ArVI] 4.53 μm (panel b), [MgIV] 4.49 μm (panel c) and [NeVI] 7.65 μm (panel d) lines, for an AGN with a total IR luminosity of $L_{\text{IR}} = 10^{12} L_{\odot}$. We chose this luminosity because it better represents the population at the knee of the luminosity function for galaxies at redshift $z \lesssim 3$. For comparison, this figure and the following ones include also the sensitivity of the SPICA Mid-IR Instrument (SMI; grey dashed line) that was considered for the SPICA Mission (Roelfsema et al. 2018; Spinoglio et al. 2021a; Kaneda et al. 2017). This comparison indicates the better sensitivity of a cryogenically cooled space telescope at long wavelengths ($\lambda > 15 \mu\text{m}$), even of smaller diameter, such as the one of the SPICA project (2.5 m), as compared to the JWST.

Considering an integration time of 1 h and a signal to noise ratio of $\text{SNR}=5$, MIRI will be able to detect the [NeV] line up to redshift $z \sim 0.8$. The [ArVI] line can be observed up to redshift $z \sim 1.8$ for objects with an ionization parameter of $\log U = -1.5$, almost independently of the gas density, while objects with lower ionization can be observed up to redshift $z \sim 1$. The [MgIV] line can be observed up to redshift $z \sim 1.8$ for objects with an ionization parameter of $\log U = -1.5$, independently of the gas density. An ionization parameter of $\log U = -2.5$ extends the observational limit to a redshift of $z \sim 2.8$. The [NeVI] 7.65 μm line can be observed up to redshift $z \sim 1.2$ for objects with an ionization parameter of $\log U = -2.5$, independently of gas density. However, for a higher ionization parameter of $\log U = -1.5$ and a gas density of $\log(n_{\text{H}}/\text{cm}^{-3}) = 2$, this line can be detected up to redshift $z \sim 1.5$, and up to redshift $z \sim 1.6$ if the gas density is $\log(n_{\text{H}}/\text{cm}^{-3}) = 4$.

Satyapal et al. (2021), performing similar simulations, assume different physical parameters. In particular, these authors fix the

hydrogen density to the value of $\log(n_{\text{H}}/\text{cm}^{-3}) = 2.5$, and assume a ionization parameter either equal to $\log U = -1$ or -3 . We obtain, however, similar results, with the [MgIV] line which results to be the strongest tracer in low ionization AGN, while the [NeVI] line dominates the AGN spectra at higher ionizations.

Figures 4 and 5 show the predicted fluxes for a SFG and a LMG, respectively, with total IR luminosity of $L_{\text{IR}} = 10^{12} L_{\odot}$, as a function of redshift, compared to the MIRI sensitivity, of the [NeII] 12.8 μm (panel a), [ArII] 6.98 μm (panel b) and [ArIII] 8.99 μm (panel c) lines. For the SFG, the [NeII] line can be detected up to redshift $z \sim 1$ with a 1 h observation, while the [ArII] line can be observed up to redshift $z \sim 1.5$ for models with an ionization parameter of $\log U = -2.5$, while for $\log U = -3.5$ the limiting redshift is increased to $z \sim 2.2$. For the [ArIII] line, the limiting redshift is of $z \sim 1.2$ independently of the adopted model.

For the LMG, the simulation yields similar results. Considering a source of total IR luminosity of $L_{\text{IR}} = 10^{12} L_{\odot}$, the [NeII] line can be detected up to $z \sim 1.25$; the [ArII] line can be detected up to $z \sim 1.5$ independently of the adopted model. For the [ArIII] line, the maximum redshift is reached for an ionization parameter of $\log U = -2$, and is equal to $z \sim 2$, while for an ionization parameter of $\log U = -3$ the maximum redshift is of $z \sim 1.7$, independent of gas density.

Figure 6 shows the predicted fluxes for both a SFG and LMG with total IR luminosity $L_{\text{IR}} = 10^{12} L_{\odot}$, as a function of redshift, compared to the MIRI sensitivity, of the PAH features at 6.2 and 7.7 μm (panels a and b, respectively), and of the [SIV] 10.5 μm line (panel c). Given the high intensity of the PAH features, these can be easily detected by MIRI up to redshift $z \sim 3.6$ for the 6.2 μm feature, and up to redshift $z \sim 2.7$ for the 7.7 μm feature. The [SIV] line can be observed up to redshift $z \sim 1.7$, requiring longer integration times to be detected in SFG above redshift $z \sim 0.8$.

In all simulations, the decrease in sensitivity of MIRI in the 16–29 μm observed spectral range increases the required exposure times to values much longer than 1 h, in order to detect sources at higher redshift and thus probe the highly obscured galaxies at the Cosmic noon.

3.2. Predictions for ALMA

In this section we compare the predicted flux of the [OI] 63 and 145 μm , [OIII] 88 μm , [NII] 122 and 205 μm and [CII] 158 μm lines as a function of redshift to the sensitivity that the ALMA telescope can achieve in 1 and 5 h observations, in order to determine the limits of the instrument in studying galaxy evolution through cosmic time.

Figure 7 shows the atmospheric transmission at the ALMA site on Llano de Chajnantor. The transmission curve is obtained from the atmospheric radiative transfer model for ALMA by Pardo (2019), and covers the 85–950 GHz frequency interval, equivalent to the 300 μm to 3.6 mm wavelength range. The figure shows the zenith atmospheric transmission for a precipitable water vapour (PWV) of 2.0, 1.0 and 0.5 mm. The PWV indicates the depth of water in the atmospheric column, if all the water in that column were measured as rainfall in mm. The PWV at the ALMA site is typically below 2.0 mm for 65% of the year, below 1.0 mm for 50% of the time and goes below 0.5 mm for 25% of the time. Bands at higher frequencies (Bands 9 and 10) are more affected by atmospheric transmission: considering a PWV of 1.0 mm, the atmospheric transmission is $\sim 30\%$ at 850 GHz (Band 10). Going

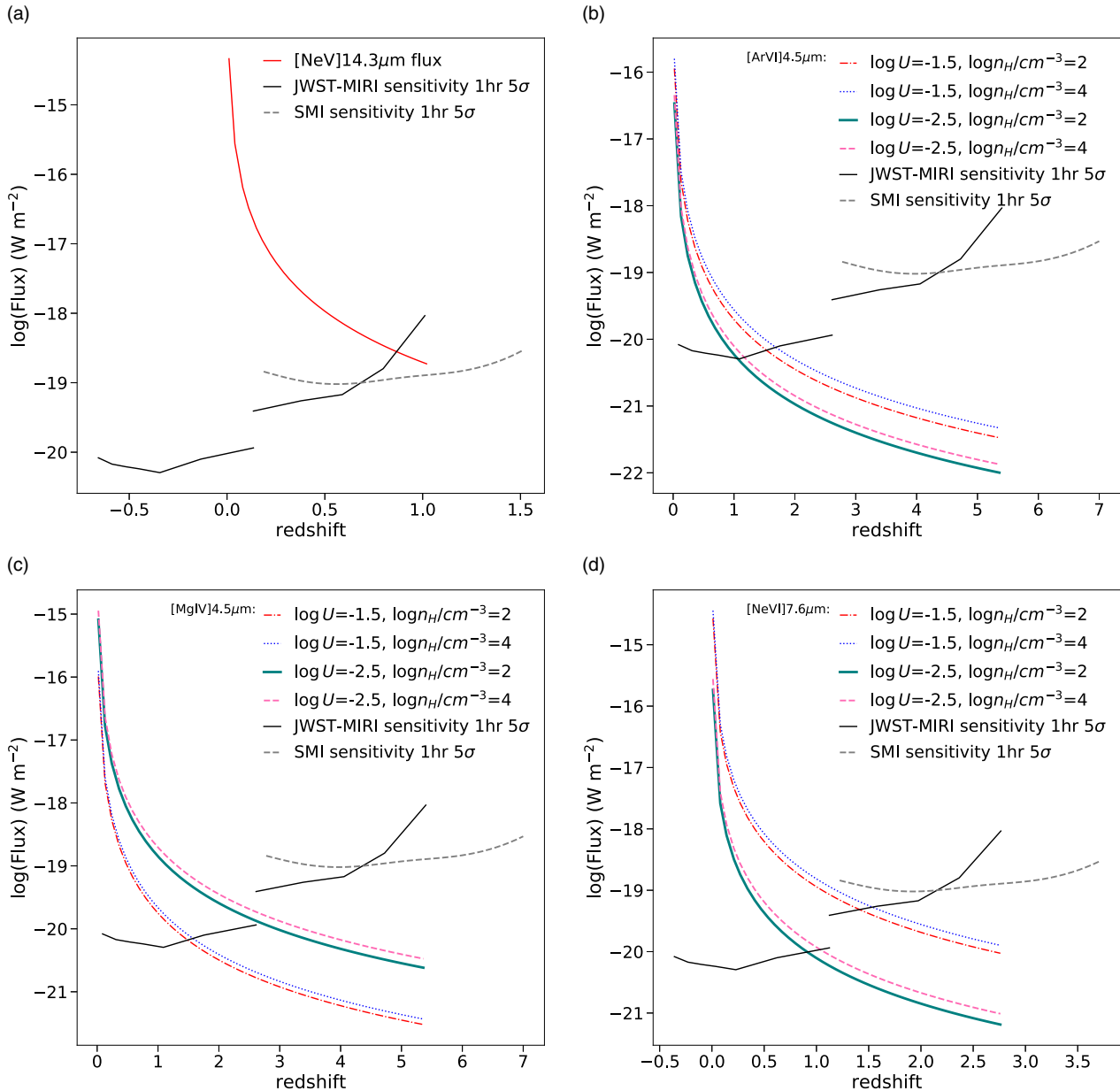


Figure 3. Predicted fluxes, as a function of redshift, for an AGN with a total IR luminosity of $L_{IR} = 10^{12} L_{\odot}$ for the [NeV]14.3 μm (a:top left, red solid line); the [ArVI]4.5 μm line (b:top right); the [MgIV]4.49 μm line (c:bottom left) and for the [NeVI]7.65 μm line (d: bottom right). In all figures, the black solid line shows the 1 h, 5σ sensitivity of JWST-MIRI, while the grey dashed line shows the 1 h, 5σ sensitivity of the SPICA SMI-LR (Kaneda et al. 2017). In panels b, c and d, the red dash-dotted line shows the predicted flux for a galaxy with an ionization parameter of $\log U = -1.5$ and a hydrogen density of $\log(n_H/\text{cm}^{-3}) = 2$, the blue dotted line indicates $\log U = -1.5$ and $\log(n_H/\text{cm}^{-3}) = 4$, the green solid line shows $\log U = -2.5$ and $\log(n_H/\text{cm}^{-3}) = 2$, and the pink dashed line shows $\log U = -2.5$ and $\log(n_H/\text{cm}^{-3}) = 4$.

toward shorter frequencies, the transmission goes up to $\sim 50\%$ at 550 GHz (Band 8), and $\sim 90\%$ below 300 GHz (Bands 3–6).

When determining the integration time using the ALMA sensitivity calculator,¹ the PWV is automatically selected by the online tool to the most representative value for each band of observation.

As can be seen from Figures 8 to 10 it has to be noticed that the ALMA sensitivity as a function of redshift is not a simple monotonic function, but contains discontinuities due to atmospheric absorption at particular frequencies. These figures show

the fluxes predicted for various lines as a function of redshift for a source of total IR luminosity of $L_{IR} = 10^{12.5} L_{\odot}$, compared to the ALMA sensitivity in 1 and 5 h reaching a signal-to-noise $\text{SNR}=5$, assuming the line calibrations for SFG, LMG and AGN presented in Mordini et al. (2021). Where available, we have included in the figures the detections so far reported in high redshift galaxies (indicated as yellow stars: \star). For predicting the fluxes at each redshift, we have chosen the luminosity of $L_{IR} = 10^{12.5} L_{\odot}$ because it corresponds to the luminosity of a Main-Sequence (MS) galaxy of mass of $M_{\star} = 10^{10.7} M_{\odot}$ at a redshift $z = 4$ (Scoville et al. 2017). This allows us to predict the observability of galaxies at the knee of the luminosity and mass function at redshift $z \gtrsim 3$.

¹<https://almascience.eso.org/proposing/sensitivity-calculator>.

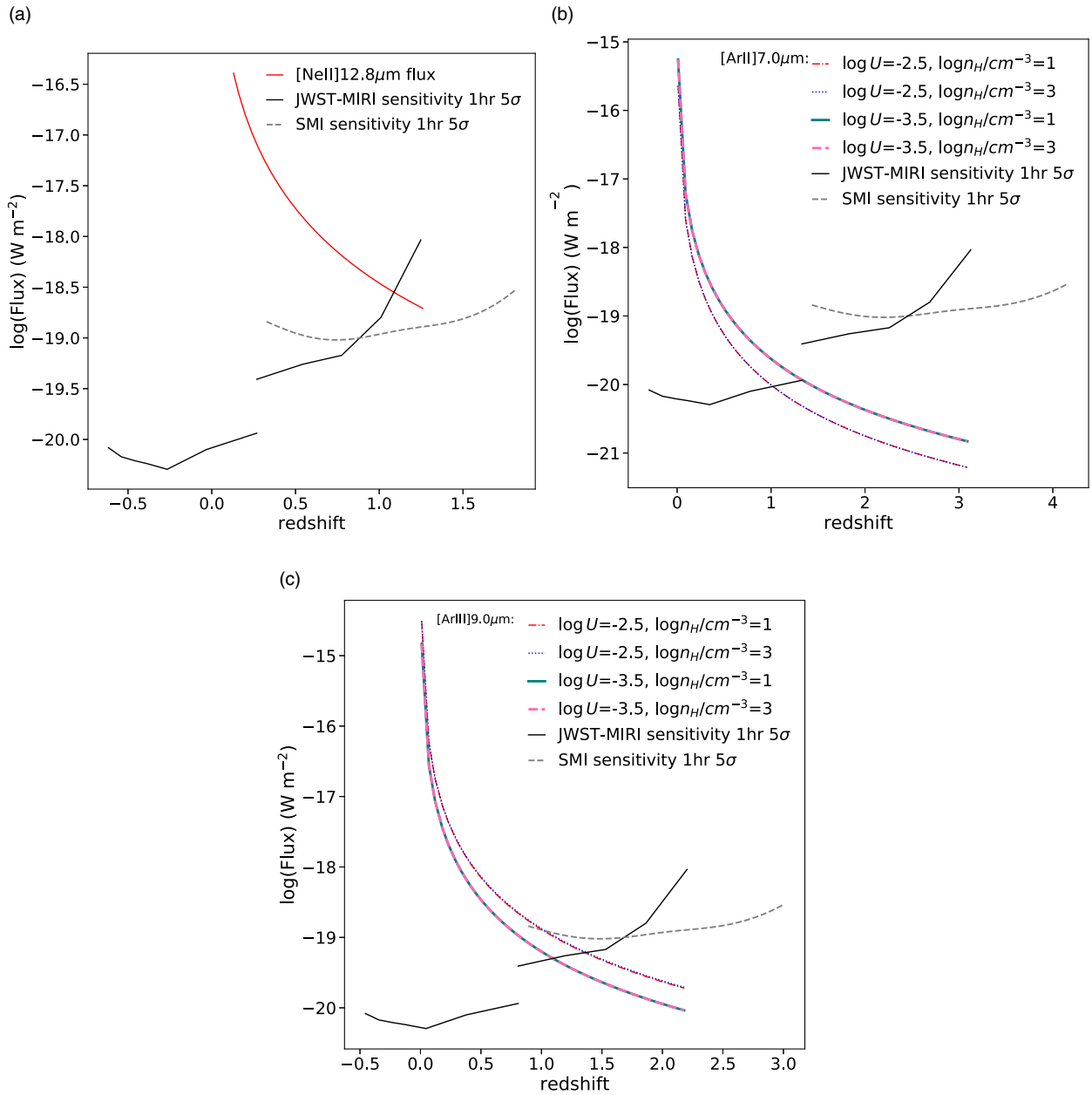


Figure 4. Predicted fluxes, as a function of redshift, of a SFG with a total IR luminosity of $L_{IR} = 10^{12} L_{\odot}$ for the [Nell]12.8 μm (a: top left, red solid line); [ArII]6.98 μm line (b: top right) and for the [ArII]8.99 μm line (c: bottom). In all figures, the black solid line shows the 1 h, 5 σ sensitivity of JWST-MIRI, while the grey dashed line shows the 1 h, 5 σ sensitivity of the SPICA SMI-LR (Kaneda et al. 2017). In panels b and c, the red dash-dotted line shows a galaxy with an ionization parameter of $\log U = -2.5$ and a hydrogen density of $\log(n_H/\text{cm}^{-3}) = 1$, the blue dotted line indicates $\log U = -2.5$ and $\log(n_H/\text{cm}^{-3}) = 3$, the green solid line shows $\log U = -3.5$ and $\log(n_H/\text{cm}^{-3}) = 1$, and the pink dashed line shows $\log U = -3.5$ and $\log(n_H/\text{cm}^{-3}) = 3$.

In Figure 8, we show the fluxes predicted for the [OI]63 μm (top) and [OIII]88 μm (bottom) lines as a function of redshift. The [OI]63 μm line could in principle be observed by ALMA starting from the redshift of $z \sim 4$ and up to a redshift of $z \sim 8$. However, the line is observable only using ALMA bands 9 and 10, making it rather difficult to detect, due to the low atmospheric transmission. Considering the LMG calibration, the line would require an integration time of ~ 5 h to be detected, while for the SFG and AGN calibrations the observational time would be between 10 and 20 h. This value is unrealistic for a ground-based telescope, such as ALMA, and in principle could be achieved only by summing

up the results of various observing runs of few hours each. As a matter of fact, the only detection of the [OI]63 μm line available so far for a high-redshift galaxy is the one reported by Rybak et al. (2020), shown in the figure, for a strongly gravitationally lensed galaxy (magnification $\mu_{FIR} \simeq 9$) obtained with the APEX 12 m telescope (Güsten et al. 2006), and the Swedish ESO PI (SEPIA) Band 9 receiver (Belitsky et al. 2018).

The [OIII]88 μm line, on the other hand, can be observed from redshift $z \sim 3$. For this line, galaxies that present physical characteristics similar to local LMG can be easily detected with observations shorter than 1 h, while for SFG and AGN, observational

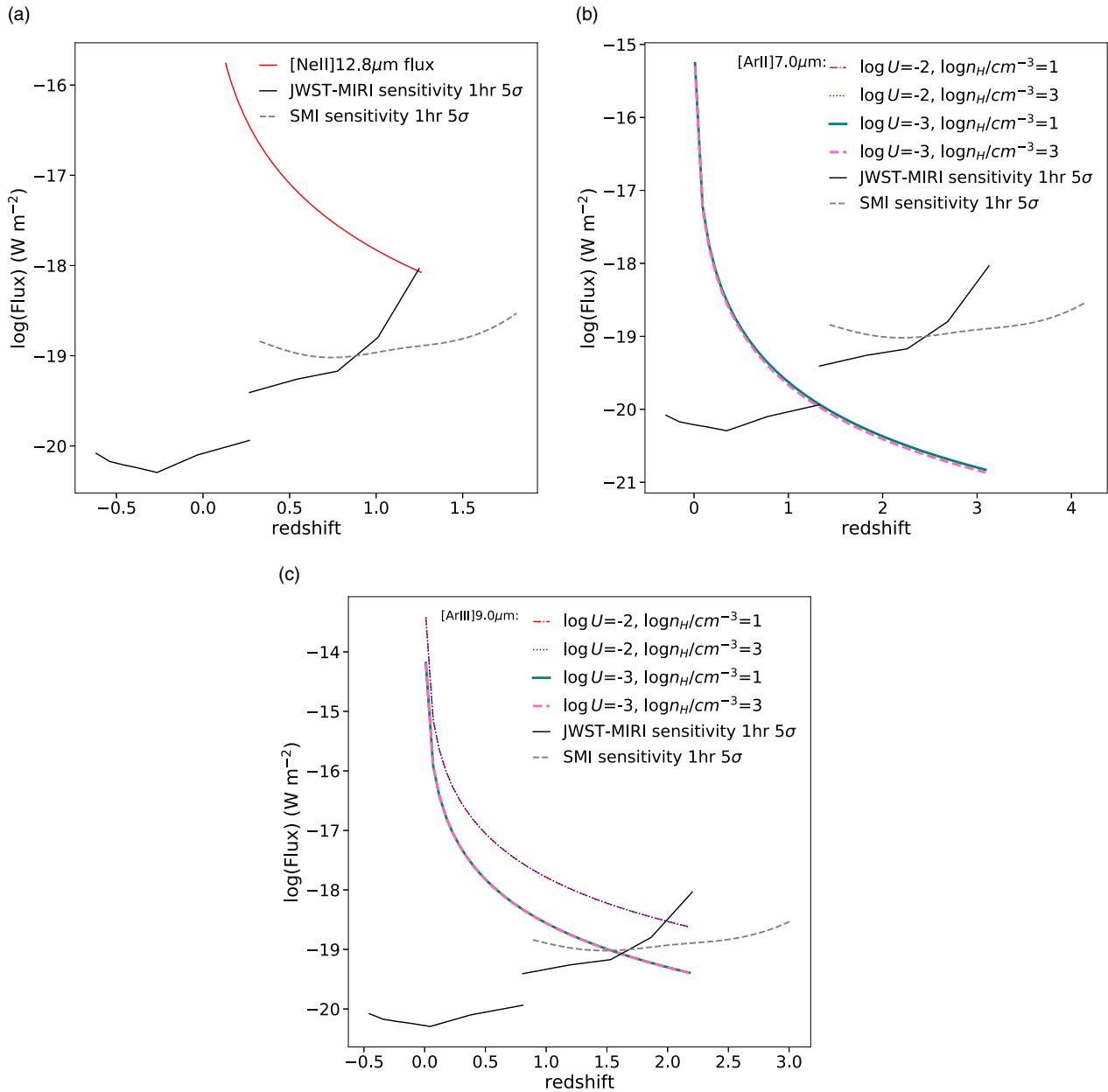


Figure 5. Predicted fluxes, as a function of redshift, of a LMG with a total IR luminosity of $L_{\text{IR}} = 10^{12} L_{\odot}$ for the [NeII]12.8 μm (a: top left, red solid line); the [ArII]6.98 μm line (b: top right) and the [ArIII]8.99 μm line (c: bottom). In all figures, the black solid line shows the 1 h, 5 σ sensitivity of JWST-MIRI, while the grey dashed line shows the 1 h, 5 σ sensitivity of the SPICA SMI-LR (Kaneda *et al.* 2017). In panels b and c, the red dash-dotted line shows a galaxy with an ionization parameter of $\log U = -2$ and a hydrogen density of $\log(n_{\text{H}}/\text{cm}^{-3}) = 1$, the blue dotted line indicate $\log U = -2$ and $\log(n_{\text{H}}/\text{cm}^{-3}) = 3$, the green solid line shows $\log U = -3$ and $\log(n_{\text{H}}/\text{cm}^{-3}) = 1$, and the pink dashed line shows $\log U = -3$ and $\log(n_{\text{H}}/\text{cm}^{-3}) = 3$.

times longer than 5 h are required up to redshift $z \sim 8$. In the figure, we report the [OIII]88 μm detections by Vishwas *et al.* (2018), Walter *et al.* (2018), De Breuck *et al.* (2019), Tamura *et al.* (2019), Harikane *et al.* (2020). We note that, while all reported detections have signal to noise ratio of $\text{SNR} = 5$ or higher, the integration times can reach values of the order of 7.5 h. Moreover, we do not correct the line luminosities for the magnification effect, when present.

In Figure 9, we show the fluxes predicted for the [NII]122 μm (top) and [OI]145 μm (bottom) lines as a function of redshift. In AGN, the [NII] line can be detected with an integration time of

less than 1 h, from a redshift of $z \sim 1.8$. For SFG, the line can be detected with observations of the order of 5 h only for redshifts above $z \sim 6$, while at lower redshifts, or for LMG, the observational times needed to detect this line are longer than 5 h. The [OI]145 μm line can be observed with integration times of the order of 5 h above redshift $z \sim 4$ in SFG and LMG, while in AGN or for lower redshifts, longer integration times are needed. In the figure, we also report a detection for [NII]122 μm and [OI]145 μm (De Breuck *et al.* 2019).

It is important to note, when considering nitrogen and oxygen lines, that the proposed predictions are derived for local

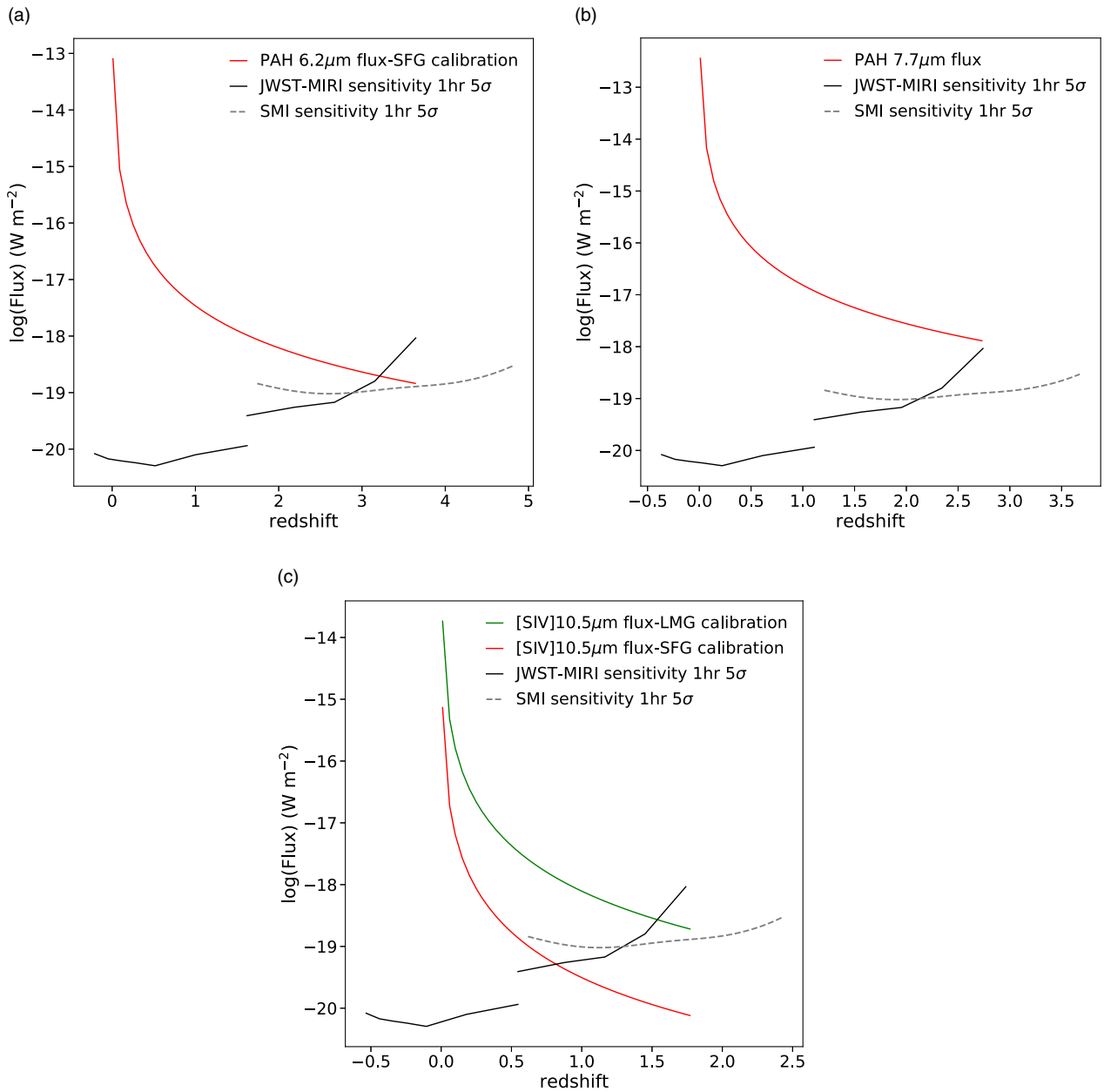


Figure 6. Predicted fluxes, as a function of redshift, of a source with a total IR luminosity of $L_{IR} = 10^{12} L_{\odot}$ for the 6.2 μm PAH feature (a:top left); the 7.7 μm PAH feature (b:top right) and for the [SIV]10.5 μm line considering the SFG calibration (red solid line) and the LMG calibration (green solid line) (c:bottom). In all figures, the black solid line shows the 1 h, 5 σ sensitivity of JWST-MIRI, while the grey dashed line shows the 1 h, 5 σ sensitivity of the SPICA SMI-LR (Kaneda et al. 2017).

galaxies, where the nitrogen to oxygen ratio shows typically values of about $\log(N/O) \sim -0.6$ (Pilyugin et al. 2014). When considering high redshift objects, however, this ratio may vary (e.g. Amorín, Pérez-Montero, & Vázquez 2010), since it depends, among other parameters, on the stellar initial mass function, the star formation efficiency, and the star formation history due to the secondary origin of nitrogen in the CNO cycle in intermediate-mass stars. For this reason, while the detections of high redshift objects are in agreement with our calibration, different N/O ratios from the solar value $\log(N/O) \sim -0.6$ would introduce an additional scatter in the calibration of the nitrogen lines for galaxies at high redshift.

Finally, Figure 10 shows the predicted fluxes for the [CII]158 μm (top) and the [NII]205 μm (bottom) lines. The [CII] line is by far the brightest far-IR fine-structure line in galaxies and given its longer wavelength it can be detected in the redshift ranges of $0.9 \lesssim z \lesssim 2$ and $3 \lesssim z \lesssim 9$, requiring integration times shorter than 1 h independently of the galaxy type. The [NII]205 μm line can be detected from redshift $z \sim 0.5$, however it requires at least 1 h of observation up to $z \sim 3$, and a longer integration at higher redshifts for SFG. For AGN the line appears weaker, and requires integration times longer than 5 h to be detected. We include the detections for the [CII]158 μm line reported by Faisst et al.

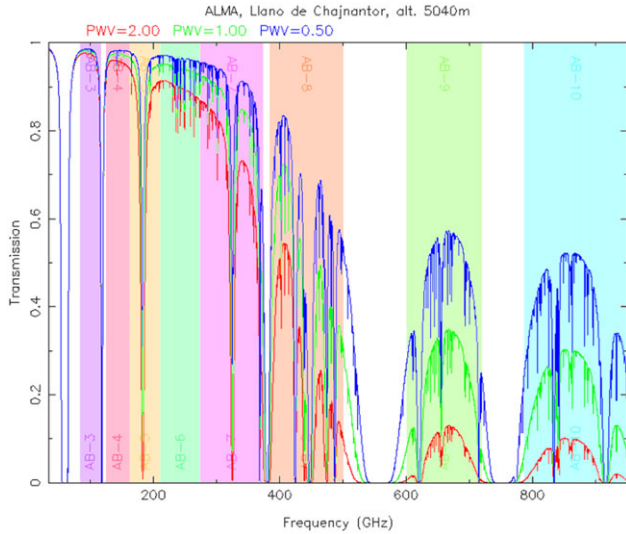


Figure 7. Atmospheric transmission at the ALMA site on Llano de Chajnantor, at different frequencies, for three values of precipitable water vapour (PWV): 2.0 mm (red), 1.0 mm (green) and 0.5 mm (blue). The vertical shaded areas show the frequency coverage of the different ALMA Bands, from AB-3 to AB-10. Prediction obtained with the on-line calculator at <https://almascience.nrao.edu/about-almata/atmosphere-model>.

(2020), Venemans et al. (2020) and for the [NII]205 μm line by Cunningham et al. (2020), considering only objects with signal to noise ratio of SNR=5 or higher.

We note here that, while in our calculations we have considered a source with a total IR luminosity of $L_{\text{IR}} = 10^{12.5} L_{\odot}$, brighter galaxies, or sources whose apparent flux is enhanced by gravitational lensing, can be detected in shorter integration times.

4. Measuring the SFR and the black hole accretion rate

We derive here the prescriptions to measure the SFR and the BHAR with the JWST-MIRI spectrometer at the Cosmic Noon ($1 \lesssim z \lesssim 3$), and the SFR with ALMA at higher redshift ($z \gtrsim 3$).

For the JWST predictions, we follow the same method that has been prepared for the scientific assessment of the galaxy evolution observational program (Spinoglio et al. 2021a) for the SPICA mission (Roelfsema et al. 2018). In this study, the predictions of measuring the SFR and the BHAR with the 2.5 m SPICA telescope have been carried out using the [NeII]12.8 μm and [NeIII]15.6 μm lines for the SFR and [OIV]26 μm for the BHAR (see Figure 9 of Spinoglio et al. 2021a), while for JWST-MIRI we use shorter wavelength lines.

Figure 11(a) shows the SFR of a galaxy in the Main Sequence (MS; Rodighiero et al. 2010; Elbaz et al. 2011), with values of luminosities as a function of redshift taken from Scoville et al. (2007), assuming a galaxy with a stellar mass of $M_{\star} = 10^{10.7} M_{\odot}$ (Muzzin et al. 2013; Adams et al. 2021) and an associated dispersion around the MS of 0.35 dex (red shaded area; Schreiber et al. 2015). The relation between luminosity and SFR has been taken from Kennicutt & Evans (2012). The various colored lines indicate the JWST-MIRI sensitivity limit for a 1 h pointed observation, considering the PAH features at 6.2 and 7.7 μm for SFG and the [ArIII]8.99 μm line for both SFG and LMG, as discussed in Section 3.1. For the PAH features, we considered the calibrations of Mordini et al. (2021), while for the [ArIII] line calibration we adopted the higher line ratio to the [NeII] line, whose calibration is given in Mordini et al. (2021), reported in Table 2, and thus

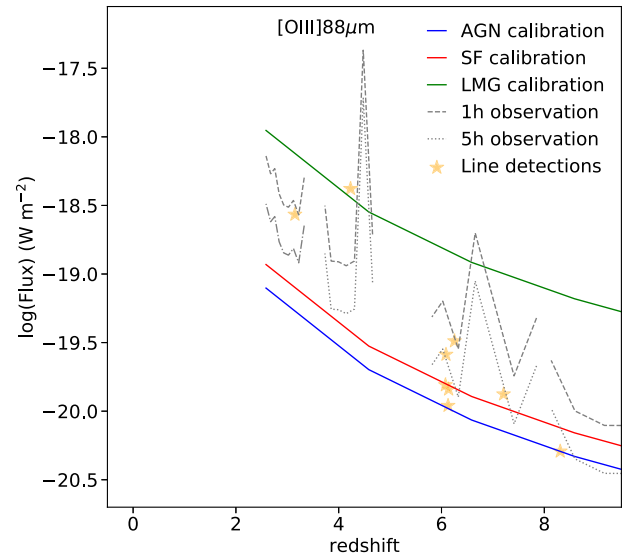
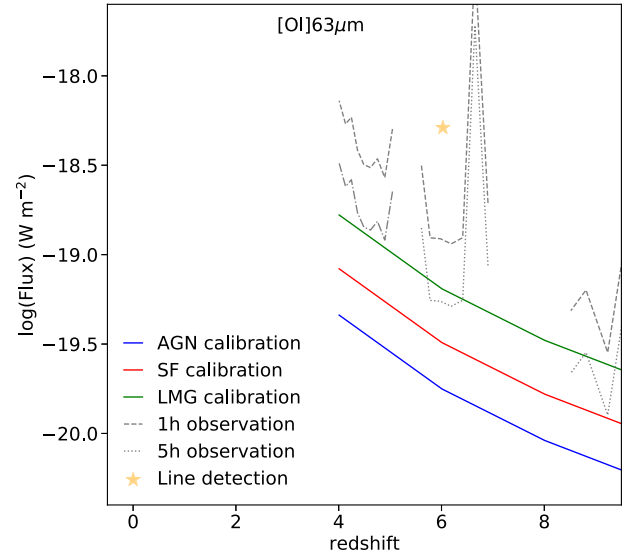


Figure 8. Predicted fluxes as a function of redshift for the [OI]63 μm line (top) and the [OIII]88 μm line (bottom), compared to the ALMA sensitivity for a 1 h (grey dashed line) and for a 5 h observation (grey dotted line) up to redshift $z \sim 9$. The blue solid line shows the predicted flux using the calibration for local AGN, the red line with the calibration for local SFG, and the green solid line with the one for local LMG. The various atmospheric absorption peaks show redshift intervals that cannot be observed. The orange stars show detections for each line.

the physical conditions yielding the brightest lines. The PAH features at 6.2 and 7.7 μm are the best tracers for the SFR, covering the population below the MS up to redshift $z \sim 3$, with a minimum luminosity of $L_{\text{IR}} \sim 10^{9.5} L_{\odot}$ at $z \sim 1$ and $L_{\text{IR}} \sim 10^{12.5} L_{\odot}$ at $z \sim 3$. The [ArIII]8.99 μm line, on the other hand, can be detected in MS galaxies up to redshift $z \sim 1.8$ (limiting luminosities between $L_{\text{IR}} \sim 10^{11} L_{\odot}$ at $z \sim 1$ and $L_{\text{IR}} \sim 10^{13} L_{\odot}$ at $z \sim 2.2$). This poses a limit to the study of LMG at higher redshifts, since the reduced formation efficiency and the increased stellar radiation hardness reduces the strength of the PAH features in these galaxies, which, in the local universe, are only detected at metallicities above 1/8-1/10 Z_{\odot} (Engelbracht et al. 2008; Cormier et al. 2015; Galliano et al. 2021).

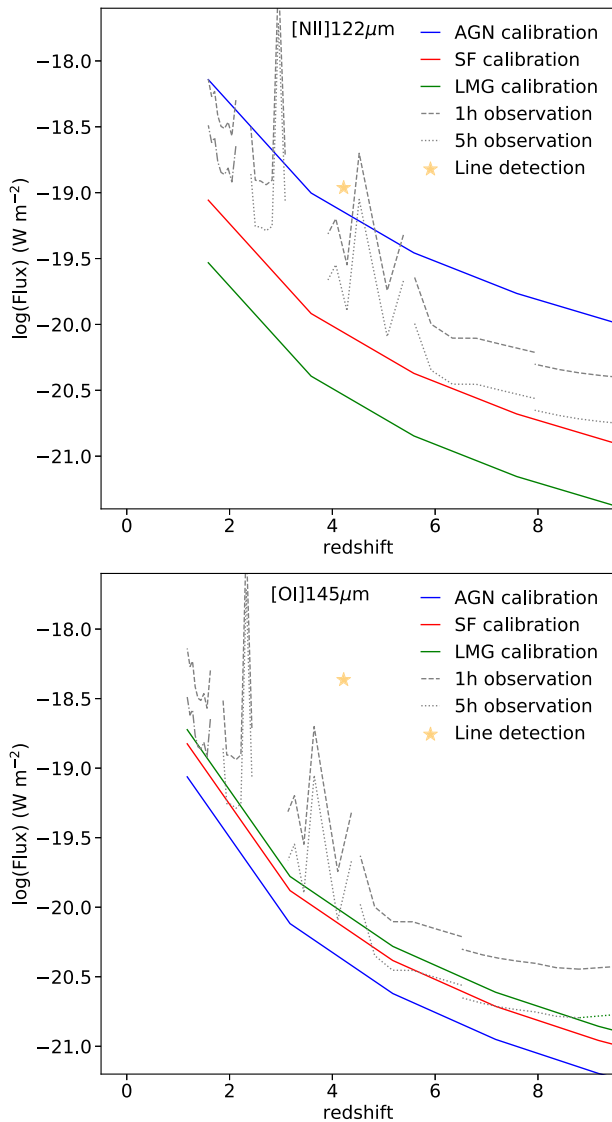


Figure 9. Predicted fluxes as a function of redshift for the [NII]122 μm line (top) and the [OI]145 μm line (bottom), compared to the ALMA sensitivity for a 1 h (grey dashed line) and for a 5 h observation (grey dotted line) up to redshift $z \sim 9$. The blue solid line shows the predicted flux considering the calibration for local AGN, the red line shows the calibration for local SFG, and the green solid line shows the calibration for local LMG. The orange stars show detections for each line.

The results presented for the ALMA telescope suggest that the [CII]158 μm line, a proxy for measuring the SFR, can be easily observed in objects at redshift $z \gtrsim 3$, thus allowing to trace the evolution of SFR throughout cosmic time. At the present time, this line has been observed by ALMA in the $z \sim 4\text{--}7$ redshift interval (see e.g. Hashimoto et al. 2019; Faisst et al. 2020). An alternative can be offered by the sum of the [OIII]88 μm and [OI]145 μm lines, in analogy to the [OI]63 μm plus [OIII]88 μm tracer proposed in Mordini et al. (2021). Because of its longer wavelength, the [OI]145 μm line is not affected by the strong atmospheric absorption that makes very difficult the observations of the [OI]63 μm line, as shown in Figures 8 and 9. The [OI]145 μm can be detected with ALMA above redshift $z \sim 1.5$ with observations of ~ 5 h for SFG and LMG-like sources, and,

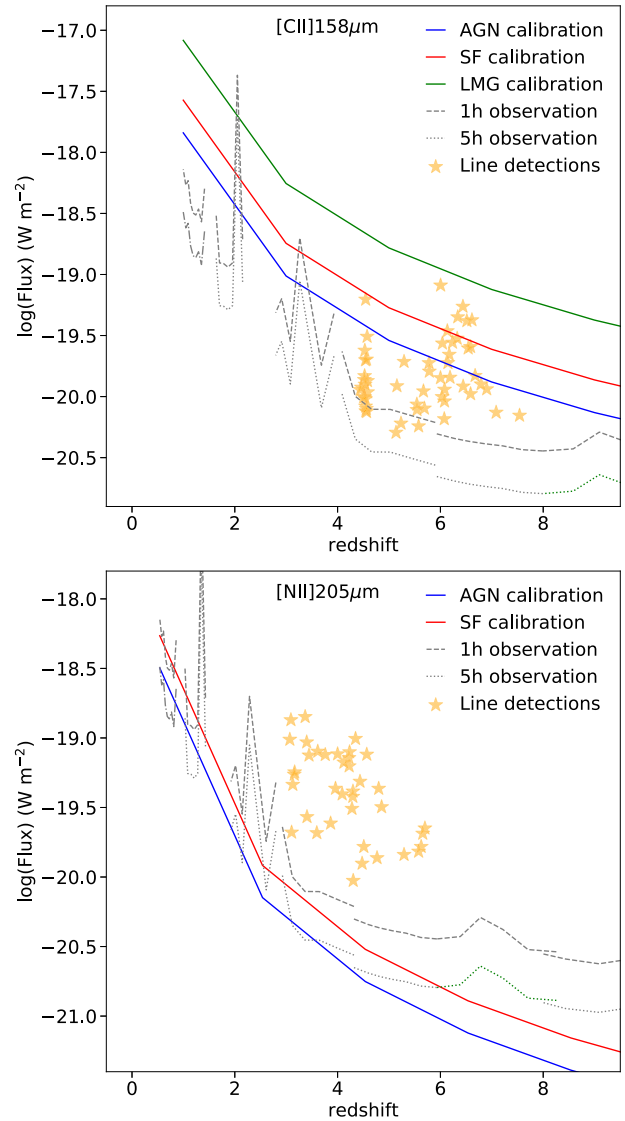


Figure 10. Predicted fluxes as a function of redshift for the [CII]158 μm line (top) and the [NII]205 μm line (bottom), compared to the ALMA sensitivity for a 1 h observation (grey dashed line) and for a 5 h observation (grey dotted line) up to redshift $z \sim 9$. The blue solid line shows the predicted flux considering the calibration for local AGN, the red line shows the calibration for local LMG. The orange stars show detections for each line.

unlike the [OI]63 μm line, is not affected by self-absorption (see, e.g., Liseau, Justanont, & Tielens 2006).

We report here the correlations between the SFR and the PAH 6.2 μm feature luminosity (Equation (1)), that can be observed by the JWST-MIRI, and between the SFR and the [CII]158 μm line luminosity (Equation (2)), currently observed by ALMA, derived by Mordini et al. (2021):

$$\log\left(\frac{\text{SFR}}{M_{\odot} \text{ yr}^{-1}}\right) = (0.37 \pm 0.04) + (0.76 \pm 0.03) \log\left(\frac{L_{\text{PAH}6.2}}{10^{41} \text{ erg s}^{-1}}\right) \quad (1)$$

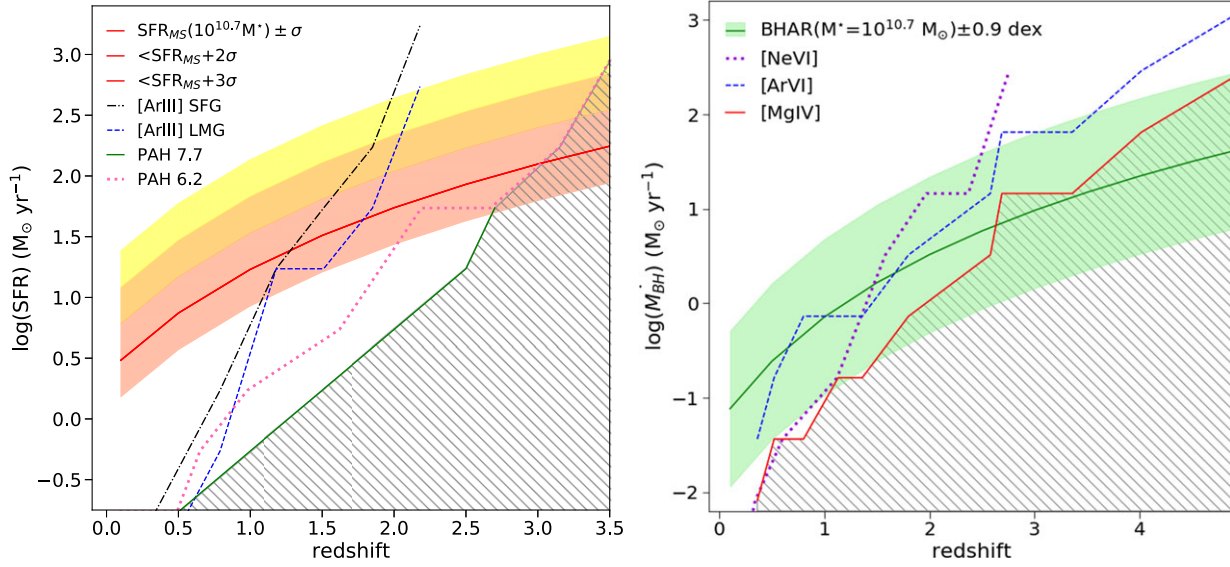


Figure 11. (a: left) Star formation rate (SFR, in $M_{\odot} \text{ yr}^{-1}$) as a function of redshift for a $10^{10.7} M_{\odot}$ galaxy in the Main Sequence (MS, Scoville et al. 2017) as a red solid line. The red-shaded area shows the $\sigma = 0.35$ dex intrinsic scatter around the MS (Schreiber et al. 2015), while the dark- and light-orange shaded areas indicate the $+2\sigma$ and $+3\sigma$ lines above the MS, respectively. The observability limits for the lines are shown as: black dash-dotted line: [ArIII]8.99 μm for a SFG with $t_{\text{int}} = 1$ h; blue dashed line: same line for a LMG (in both cases the highest line ratio present in Table 2 was adopted); pink dotted line: the PAH feature at 6.2 μm ; green solid line: the PAH feature at 7.7 μm . In these latter cases, we derived the limit from the correlations in Mordini et al. (2021). (b: right) The green solid line indicates the instantaneous BH accretion rate (BHAR, in $M_{\odot} \text{ yr}^{-1}$) as a function of redshift expected for a MS galaxy with a mass of $10^{10.7} M_{\odot}$ during its active BH accretion phase at each epoch, using the SFR-BHAR relation of Diamond-Stanic & Rieke (2012). The green shaded area shows the associated dispersion. The observability limits for the lines are shown as: purple dotted line: the [NeVI]7.65 μm line; blue dashed line: the [ArVI]4.53 μm ; red solid line: the [MgIV]4.49 μm line. For all three lines, we considered a 1 h pointed observation, and the highest line ratio as reported in Table 2. In both panels, the grey hatched areas indicate the parameter space that requires observations longer than 1 h.

$$\log\left(\frac{\text{SFR}}{M_{\odot} \text{ yr}^{-1}}\right) = (0.62 \pm 0.02) + (0.89 \pm 0.02) \left(\log \frac{L_{\text{[CII]}}}{10^{41} \text{ erg s}^{-1}}\right) \quad (2)$$

with the line luminosities expressed in units of $10^{41} \text{ erg s}^{-1}$, and the SFR in $M_{\odot} \text{ yr}^{-1}$. We note that in local SFG, the bulk of the [CII] emission arises from neutral gas (Croxall et al. 2017), with only a minor contribution from ionized gas, as discussed also in Section 4.2. In LMG, however, PDR regions are less frequent, and the [CII] emission arises mainly from ionized regions (see e.g. Cormier et al. 2019). The two components, however, compensate each other, thus making this line an ideal tracer for star formation activity in galaxies with different ISM conditions.

In analogy with the [NeII]12.8 μm plus [NeIII]15.6 μm SFR tracer (see Section 3.2.4 in Mordini et al. 2021, for details), we derive the correlation between the SFR and the sum of the [ArII]6.98 μm and [ArIII]8.99 μm lines, considering the $([\text{ArII}]+[\text{ArIII}])/([\text{NeII}]+[\text{NeIII}])$ ratio (reported in Table 2), as computed from the photoionization models. This leads to a SFR to $([\text{ArII}]+[\text{ArIII}])$ lines luminosity correlation for SFG and LMG reported in Equations (3) and (4), respectively:

$$\log\left(\frac{\text{SFR}}{M_{\odot} \text{ yr}^{-1}}\right) = 1.2 + 0.96 \log\left(\frac{L_{[\text{ArII}]+[\text{ArIII}]}}{10^{41} \text{ erg s}^{-1}}\right) \quad (3)$$

$$\log\left(\frac{\text{SFR}}{M_{\odot} \text{ yr}^{-1}}\right) = 1.57 + 0.96 \log\left(\frac{L_{[\text{ArII}]+[\text{ArIII}]}}{10^{41} \text{ erg s}^{-1}}\right) \quad (4)$$

Here, we use the composite line ratio of $([\text{ArII}]+[\text{ArIII}])/([\text{NeII}]+[\text{NeIII}])$ instead of ratios of single lines, to be able to

cancel out the dependence on the metallicity, whose lower value compared to solar would increase the higher ionization line compared to the lower ionization one. The SFR tracer derived in this way is independent of metallicity.

In a similar way, while the single PAH feature might adequately trace SFR, a combination of two or more features can better keep into account the different conditions of the ISM of star forming regions. We propose here a combination of the 6.2+7.7 μm PAH features to measure the SFR. The calibration, derived using 139 SFG galaxies, is shown in Figure 12 and is described by the following equation:

$$\log\left(\frac{\text{SFR}}{M_{\odot} \text{ yr}^{-1}}\right) = (-0.50 \pm 0.15) + (0.94 \pm 0.06) \log\left(\frac{L_{\text{PAH6.2+7.7}}}{10^{41} \text{ erg s}^{-1}}\right) \quad (5)$$

The combination of the two PAH features can be used to measure SFR up to redshift $z \sim 2.7$.

Following Mordini et al. (2021), who proposed the use of the sum of the [OI]63 μm plus [OIII]88 μm lines luminosity as a SFR tracer, we computed, for local galaxies, a correlation between the SFR and the sum of the [OIII]88 μm plus [OI]145 μm lines luminosity. Figure 13 shows the correlation described by the equation:

$$\log\left(\frac{\text{SFR}}{M_{\odot} \text{ yr}^{-1}}\right) = (0.52 \pm 0.14) + (0.93 \pm 0.14) \log\left(\frac{L_{[\text{OI}]+[\text{OIII}]}}{10^{41} \text{ erg s}^{-1}}\right) \quad (6)$$

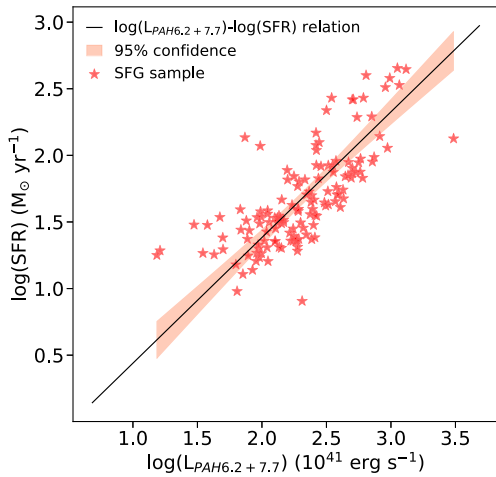


Figure 12. Correlation between the summed PAH features luminosities at 6.2 and 7.7 μm , in units of $10^{41} \text{ erg s}^{-1}$, and the SFR derived from the total IR luminosity (black solid line) for a sample of SFGs (red stars). See Section 2 in Mordini et al. (2021) for details on the sample.

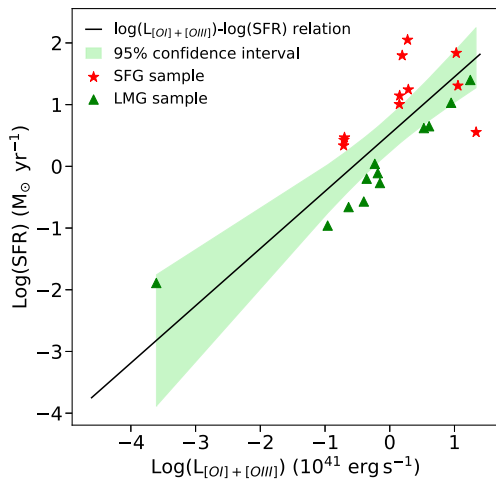


Figure 13. Correlation between the [OIII]88 μm and [OI]145 μm summed emission line luminosities, in units of $10^{41} \text{ erg s}^{-1}$, and the SFR derived from the total IR luminosity (black solid line) for a composite sample of SFGs (red stars) and from the $\text{H}\alpha$ luminosity (corrected for the IR luminosity) for LMG (green triangles). See section 3 in Mordini et al. (2021) for details on the determination of the SFR.

The correlation was obtained using 23 local galaxies, of which 11 SFG (from Negishi et al. 2001) and 12 LMG (from Cormier et al. 2015), and has a Pearson r coefficient of 0.77. The relatively small number of objects used to derive this correlation is due to the few detections of the [OI]145 μm line in local galaxies, which broadens the confidence interval of the relation, reported in Figure 13 as a shaded area.

Figure 11(b) shows the instantaneous BHAR, that can be measured by JWST-MIRI, as a function of redshift for an AGN in a MS star-forming galaxy with $M^* = 10^{10.7} M_{\odot}$, using the SFR-BHAR calibration derived by Diamond-Stanic & Rieke (2012) for a sample of nearby Seyfert galaxies. The green shaded area corresponds to the dispersion of the SFR-BHAR relation, i.e. ~ 0.9 dex. This estimate, however, considers only the portion of galaxies in the MS undergoing a BH accreting phase at each epoch, with the instantaneous BHAR that has not been averaged over the duty cycle

of the active nucleus. The dashed lines represent the three proposed tracers for BHAR in Section 3.1, considering a 1 h pointed observation: the [MgIV]4.49 μm line appears to be the best tracer for BHAR, reaching galaxies below the main sequence up to redshift $z \sim 2.5$ (observable luminosities between $L_{\text{IR}} \sim 10^{10.5} L_{\odot}$ at $z \sim 1$ and $L_{\text{IR}} \sim 10^{12.5} L_{\odot}$ at $z \sim 4$). The possibility of detecting the [ArVI] and [NeVI] lines only in bright galaxies is due to the higher ionization potential needed to excite these lines (respectively of 80 and 126 eV, see Table 1).

It is important to consider that the lines analyzed in this work have not been extensively observed yet, and these predictions are based on CLOUDY photo-ionization models. Considering the line ratios reported in Table 2 and the BHAR-[NeV]14.3 μm correlation derived in Mordini et al. (2021) (see Section 3.3 and Appendix C there for details on the derivation of the correlation), we obtain a correlation between the BHAR and the [MgIV]4.49 μm line (reported in Equation (7)), and between the BHAR and the [ArVI]4.53 μm line (reported in Equation (8)).

$$\log\left(\frac{\dot{M}_{\text{BH}}}{M_{\odot} \text{ yr}^{-1}}\right) = -0.85 + 1.04 \log\left(\frac{L_{[\text{MgIV}]4.49}}{10^{41} \text{ erg s}^{-1}}\right) \quad (7)$$

$$\log\left(\frac{\dot{M}_{\text{BH}}}{M_{\odot} \text{ yr}^{-1}}\right) = 0.58 + 1.04 \log\left(\frac{L_{[\text{ArVI}]4.53}}{10^{41} \text{ erg s}^{-1}}\right) \quad (8)$$

The hatched areas in both panels of Figure 11 indicate the region where observations longer than 1 h are required. A longer exposure time can significantly improve these limits, allowing the JWST-MIRI spectrometer to study both SFR and BHAR in MS galaxies up to redshift $z \sim 3$.

Among the far-IR lines covered by the ALMA telescope at redshifts higher than $z \sim 3$, the only available tracers for BH activity are represented by the [OIII]52 and 88 μm lines. Their ionization potential (~ 35 eV, see Table 1) is sufficiently high to be excited by AGN. However, these lines are also associated to stellar and HII regions excitation, thus limiting their potential as BHA tracer. A large set of observed far-IR lines and specific photo-ionization models that could simulate the two emission components (see, e.g. Spinoglio et al. 2005, for the case of NGC1068) are needed to disentangle the stellar emission from the total observed emission of these lines.

4.1. Applications to composite objects

The coexistence of AGN and star formation in galaxies is well known (see, e.g. Pérez-Torres et al. 2021, for a review) and therefore it should be expected that many galaxies are characterized by both components at work together. The high ionization lines considered in this work can only be produced by AGN activity, and can be used in composite objects to derive the BHAR. Mid-ionization lines, however, can be produced by both AGN and star formation activity, leading to possible overestimations of the SFR.

The combination of high- and mid-ionization lines, ideally of the same element, is necessary to estimate the relative contribution of each phenomenon to the total energy output in a galaxy. For instance, Figure 14 shows the [NeV]14.3 μm to [NeIII]15.6 μm ratio in the Tommasin et al. (2010) AGN sample. Based on this ratio, we consider that a fully AGN-dominated source corresponds to a line ratio of about [NeV]/[NeIII] ~ 0.9 , which represents the 95% percentile of the line ratio distribution (vertical red line in Figure 14). A lower line ratio indicates an increasing contribution

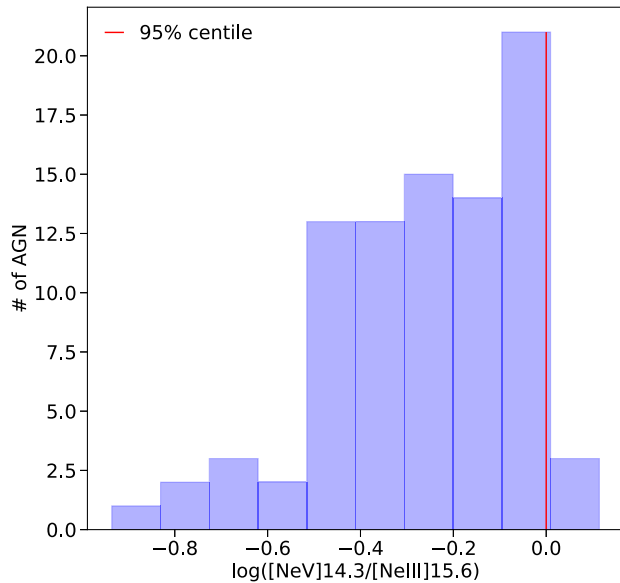


Figure 14. Histogram of the logarithm of the [NeV]14.3 μm to [NeIII]15.6 μm line for the Tommasin et al. (2010) AGN sample. The vertical red line shows the 95% percentile of the distribution.

from the star formation component, corresponds to 100% when [NeV] is not detected.

Zhuang et al. (2019), using mid-IR spectra and CLOUDY simulations, performed a similar analysis, deriving the average [NeII]12.8 μm /[NeV]14.3 μm and [NeIII]15.5 μm /[NeV]14.3 μm ratios, finding that AGN emit a relatively limited range of [NeII] and [NeIII] for a given [NeV] flux. This would allow one to predict the amount of AGN emission for these lines, and correct the observed flux in order to derive the component linked only to star formation activity.

While JWST will be able to detect both neon lines only up to redshift $z \sim 0.8$, a similar analysis could be performed using the [ArVI]4.53 and [ArIII]8.99 μm lines to reach higher redshift objects.

4.2. Other components in galaxies: PDR and shocks

In this study, we have considered so far galaxies which are dominated by an AGN, by the star formation component (SFG) and also galaxies characterized by a low metallicity (LMG) using the spectroscopy that has been collected by the *Spitzer* and *Herschel* satellites. Moreover, we have shown in the previous Section 4.1 how the AGN and SFGs can be disentangled and evaluated through the intermediate ionization lines. However, other emission components can be present in galaxies and in particular those originated in the so-called photo dissociation regions (PDR, Tielens & Hollenbach 1985) and in shocks.

To disentangle the PDR emission in galaxies from the normal photoionized component, which we expect in the presence of HII regions emission, and therefore in the presence of star formation, we can use the ratio of the [CII]158 μm line to one of the two [NII] lines, either at 122 and 205 μm . Spinoglio et al. (2015) have shown that these line ratios, together with photoionization models simulating both a starburst (with the integration stopping at the temperature of 1000 K) and a starburst plus a PDR model (with the integration going down to the temperature of 50 K, including the neutral/low ionization gas contributing

to the PDR), have a very different [CII]158 μm /[NII]122 μm and [CII]158 μm /[NII]205 μm line ratios. For the galaxies observed in Spinoglio et al. (2015) most of the [CII] emission was originated in PDR, whilst only one-fifth of the total emission was produced in pure HII regions. Thus, ALMA observations of at least one the [NII]122 205 μm lines would be required to estimate the contribution of low-density ionized gas to the [CII]158 μm emission and disentangling the PDR component.

A similar approach, albeit more complex, can be used for disentangling the presence of shock excited emission. It is in fact well known, since the pioneering works of Shull & McKee (1979), Hollenbach & McKee (1989), that dissociative shocks produce a plethora of intense atomic and ionic fine-structure lines. Notably the [OI]63 μm line intensity is proportional to the particle flux (density \times velocity) into a dissociative shock, because this line is the dominant coolant at temperature of $T \lesssim 5000$ K (Hollenbach 1985). Among the lines discussed in this study, besides [OI]63 μm , also lines of [NeII]12.8 μm , [SiII]34.8 μm , and [OIII]52 and 88 μm are present in fast dissociative shocks (Shull & McKee 1979; Hollenbach & McKee 1989). To discriminate between shocks and PDR origin the ratio of [OI]63 μm /[CII]158 μm can be used (Tielens & Hollenbach 1985), although this line ratio should be used with caution since LMG galaxies also show high [OI]63 μm /[CII]158 μm ratios (Cormier et al. 2019).

In conclusion, if one wants to disentangle shock excitation from the intensities of observed fine-structure lines in galaxies, has first to choose an adequate shock excitation model able to predict their intensities and fit the results. These detailed computations are, however, beyond the scope of the present study, whose main aim is to give simple recipes to derive from the observed lines the SFR and the BHAR.

5. Discussion

The low observational efficiency at performing wide area surveys (of the order of square degrees) with either of the two facilities, JWST and ALMA, imposes a significant limit to study galaxy evolution: while the tracers proposed in this work can be used to trace both star formation and BHA at the Cosmic Noon, a complete study of galaxy evolution also requires to account for the environment within which galaxies evolve, thus incorporating the large scale structure of the Universe, by mapping large cosmological volumes. Moreover, even using both facilities together, it is not possible to perform an accurate analysis of galaxy evolution covering both the Cosmic Noon and the higher redshifts. On the one hand, in fact, while the PAH features can be detected with JWST up to redshift $z \sim 2.5$ in MS galaxies, and at higher redshifts the ALMA telescope can trace star formation activity with the [CII]158 μm line, there is the problem of tracing SF in low metallicity environments, where the PAH features are weak or absent, or in high luminosity galaxies, where the [CII] deficit can lead to lower determinations of the SFR (see e.g. Ferrara et al. 2019). On the other hand, ALMA lacks an unambiguous tracer for BHA activity, and the proposed tracers for JWST only reach redshift $z \sim 3$ for MS galaxies.

A full characterization of the obscured phase of galaxy evolution at the Cosmic Noon will have to wait for a new IR space telescope, actively cooled down to a few degrees Kelvin and with state of the art detectors, able to perform wide area spectroscopic surveys covering most of the mid- to far-IR range (i.e. between 10

and 300 μm). Possible candidate missions include the very ambitious *Origins Space Telescope* (OST, Meixner et al. 2019) and the smaller size *Galaxy Evolution Probe* telescope (GEP, Glenn et al. 2021), which has the main goal to map the history of galaxy growth through star formation and accretion by supermassive black holes and to characterize the relationship between these two processes. The pioneering study of the scientific potential of an IR space telescope for galaxy evolution studies throughout cosmic time has been provided by Spinoglio et al. (2017); Spinoglio et al. (2021a), based on the SPICA mission project (Swinyard et al. 2009; Roelfsema et al. 2018).

6. Conclusions

In this work, we present spectroscopic tracers for star formation and BHA activity that can be used by the JWST and the ALMA telescopes to characterize galaxy evolution up to and beyond the Cosmic Noon, respectively. In particular, our findings can be summarized as follow:

- The JWST-MIRI instrument in spectroscopic mode will be able to detect mid-IR spectra of faint fine-structure lines and PAH features in galaxies at redshift $z \gtrsim 1$ and discriminate between AGN-dominated and starburst-dominated galaxies and measure their metallicity.
- The presence of an AGN can be detected using high ionization lines such as the [MgIV]4.49 μm , the [ArVI]4.53 μm or the [NeVI]7.65 μm lines: the [MgIV] and [ArVI] lines can be observed up to redshift $z \sim 3$, while the [NeVI] line can be detected with JWST-MIRI for a main-sequence galaxy at redshift $z \sim 1.5$ in a 1 h observation.
- For the star formation processes using JWST, the PAH features can be easily detected up to redshift $z \sim 2.7$, while the [ArII]6.98 μm and [ArIII]8.99 μm lines can be detected up to redshift $z \sim 2.5$ –3. The detection of the [SIV]10.5 μm line can discriminate between solar and sub-solar metallicity: in LMG, the [SIV] line can be easily detected up to redshift $z \sim 1.5$, while in solar metallicity SFG, this line is very weak and cannot be detected above redshift $z \sim 0.8$.
- Using the ALMA observatory, the far-IR oxygen lines of [OIII]88 μm and [OI]145 μm can be detected in low-metallicity galaxies (LMG) with luminosities of about $10^{12.5} L_{\odot}$ with integration times of 1–5 h. In AGN or normal SFG with similar luminosities, the [OIII]88 μm line requires $t_{\text{INT}} \gtrsim 5$ h. Due to the high observing frequency, where the sky transparency is very low, the [OI]63 μm can hardly be detected in $t_{\text{INT}} \gtrsim 5$ h and only if the galaxy is a LMG. On the contrary, the [NII]122 μm line is preferentially detected in AGN and normal star forming galaxies (SFG). The [NII]205 μm can hardly be detected with $t_{\text{INT}} \gtrsim 5$ h in AGN and SFG.
- The [CII]158 μm line can be easily detected in any main-sequence galaxy at redshift of $0.9 \lesssim z \lesssim 2$ and $3 \lesssim z \lesssim 9$. It remains the best tracer for to measure the SFR, but it can also be easily detected in AGN. Among other SFR tracers, in analogy with the proposed [OI]63 μm plus [OIII]88 μm tracer analyzed in Mordini et al. (2021), we suggest the use of the [OIII]88 μm plus [OI]145 μm for high redshift sources. The [OI]145 μm can be detected with ALMA starting from redshift $z \sim 1.5$ with observations of ~ 5 h for SFG and LMG-like sources. While in local SFG and LMG, there are not enough detections of the

[OI]145 μm line to appropriately test it as SFR tracer, this line, although fainter, should be even better than the [OI]63 μm , which can be strongly self-absorbed under certain conditions (see, e.g., Liseau et al. 2006) and should allow to measure the SFR in combination with the [OIII]88 μm line.

- The PDR contribution to the far-IR fine-structure lines in ALMA observations of high-redshift galaxies can be measured with the [CII]/[NII] line ratios, which can be then used to disentangle the PDR and the pure photoionization contributions (see, e.g., Spinoglio et al. 2015).

Finally, as a concluding remark, we emphasize the importance of using multi-feature analysis to measure both BH accretion and SFR, since individual tracers can be strongly dependent on the local ISM conditions and vary from source to source. Thus, the combination of more than one tracer provides a more robust determination of these physical quantities.

Acknowledgements. We thank the anonymous referee, who helped to improve the paper. LS and JAFO acknowledge financial support by the Agenzia Spaziale Italiana (ASI) under the research contract 2018-31-HH.0. JAFO acknowledges the financial support from the Spanish Ministry of Science and Innovation and the European Union – NextGenerationEU through the Recovery and Resilience Facility project ICTS-MRR-2021-03-CEFGA.

References

- Adams, N. J., Bowler, R. A. A., Jarvis, M. J., Häußler, B., & Lagos, C. D. P. 2021, *MNRAS*, **506**, 4933
- Álvarez-Márquez, J., et al. 2019, *A&A*, **629**, A9
- Amorn, R. O., Pérez-Montero, E., & Vlchez, J. M. 2010, *ApJ*, **715**, L128
- Armus, L., et al. 2007, *ApJ*, **656**, 148
- Bagnasco, G., et al. 2007, in Society of Photo-Optical Instrumentation Engineers (SPIE) Conference Series, Vol. 6692, *Cryogenic Optical Systems and Instruments XII*, ed. J. B. Heaney, & L. G. Burriesci, 66920M
- Belitsky, V., et al. 2018, *A&A*, **612**, A23
- Birkmann, S. M., et al. 2016, in Society of Photo-Optical Instrumentation Engineers (SPIE) Conference Series, Vol. 9904, *Space Telescopes and Instrumentation 2016: Optical, Infrared, and Millimeter Wave*, ed. H. A. MacEwen, G. G. Fazio, M. Lystrup, N. Batalha, N. Siegler, & E. C. Tong, 99040B
- Brandl, B., et al. 2021, *Msngr*, **182**, 22
- Cardelli, J. A., Clayton, G. C., & Mathis, J. S. 1989, *ApJ*, **345**, 245
- Carilli, C. L., & Walter, F. 2013, *ARA&A*, **51**, 105
- Cormier, D., et al. 2012, *A&A*, **548**, A20
- Cormier, D., et al. 2015, *A&A*, **578**, A53
- Cormier, D., et al. 2019, *A&A*, **626**, A23
- Croxall, K. V., et al. 2017, *ApJ*, **845**, 96
- Cunningham, D. J. M., et al. 2020, *MNRAS*, **494**, 4090
- De Breuck, C., et al. 2019, *A&A*, **631**, A167
- Diamond-Stanic, A. M., & Rieke, G. H. 2012, *ApJ*, **746**, 168
- Elbaz, D., et al. 2011, *A&A*, **533**, A119
- Engelbracht, C. W., et al. 2008, *ApJ*, **678**, 804
- Faisst, A. L., et al. 2020, *ApJS*, **247**, 61
- Farrah, D., et al. 2013, *ApJ*, **776**, 38
- Ferland, G. J., et al. 2017, *Rev. Mexicana Astron. Astrofis.*, **53**, 385
- Fernández-Ontiveros, J. A., et al. 2016, *ApJS*, **226**, 19
- Ferrara, A., et al. 2019, *MNRAS*, **489**, 1
- Galliano, F., et al. 2021, *A&A*, **649**, A18
- Gardner, J. P., et al. 2006, *SSR*, **123**, 485
- Gehrz, R. D., et al. 2009, *ASR*, **44**, 413
- Gilmozzi, R., & Spyromilio, J. 2007, *Msngr*, **127**, 11
- Glenn, J., et al. 2021, *JATIS*, **7**, 034004
- Goldsmith, P. F., Langer, W. D., Pineda, J. L., & Velusamy, T. 2012, *ApJS*, **203**, 13

- Greenhouse, M. A., et al. 1993, *ApjS*, **88**, 23
- Güsten, R., et al. 2006, *A&A*, **454**, L13
- Harikane, Y., et al. 2020, *ApJ*, **896**, 93
- Hashimoto, T., et al. 2019, *PASJ*, **71**, 71
- Heckman, T. M., & Best, P. N. 2014, *ARA&A*, **52**, 589
- Ho, L. C., & Keto, E. 2007, *ApJ*, **658**, 314
- Hollenbach, D. 1985, *Icar*, **61**, 36
- Hollenbach, D., & McKee, C. F. 1989, *ApJ*, **342**, 306
- Johns, M., et al. 2012, in *Society of Photo-Optical Instrumentation Engineers (SPIE) Conference Series*, Vol. 8444, Ground-based and Airborne Telescopes IV, ed. L. M. Stepp, R. Gilmozzi, & H. J. Hall, **84441H**
- Kaneda, H., et al. 2017, *PASA*, **34**, e059
- Kashino, D., et al. 2019, *ApjS*, **241**, 10
- Kennicutt, R. C., & Evans, N. J. 2012, *ARA&A*, **50**, 531
- Laporte, N., et al. 2017, *ApJ*, **837**, L21
- Launay, J. M., & Roueff, E. 1977, *A&A*, **56**, 289
- Liseau, R., Justtanont, K., & Tielens, A. G. G. M. 2006, *A&A*, **446**, 561
- Madau, P., & Dickinson, M. 2014, *ARA&A*, **52**, 415
- Madden, S. C., et al. 2013, *PASP*, **125**, 600
- Maiolino, R., et al. 2008, *A&A*, **488**, 463
- Mannucci, F., et al. 2009, *MNRAS*, **398**, 1915
- Meixner, M., et al. 2019, arXiv e-prints, [arXiv:1912.06213](https://arxiv.org/abs/1912.06213)
- Meléndez, M., et al. 2008, *ApJ*, **682**, 94
- Mordini, S., Spinoglio, L., & Fernández-Ontiveros, J. A. 2021, *A&A*, **653**, A36
- Muzzin, A., et al. 2013, *ApJ*, **777**, 18
- Negishi, T., Onaka, T., Chan, K. W., & Roellig, T. L. 2001, *A&A*, **375**, 566
- Onodera, M., et al. 2016, *ApJ*, **822**, 42
- Pardo, J. R. 2019, in *ALMA Development Workshop*, 36
- Pérez-Torres, M., Mattila, S., Alonso-Herrero, A., Aalto, S., & Efstathiou, A. 2021, *A&Ar*, **29**, 2
- Perley, R. A., Chandler, C. J., Butler, B. J., & Wrobel, J. M. 2011, *ApJ*, **739**, L1
- Pilyugin, L. S., Grebel, E. K., & Kniazev, A. Y. 2014, *AJ*, **147**, 131
- Rieke, G. H., et al. 2015, *PASP*, **127**, 584
- Rodighiero, G., et al. 2010, *A&A*, **515**, A8
- Roelfsema, P. R., et al. 2018, *PASA*, **35**, e030
- Rybak, M., Zavala, J. A., Hodge, J. A., Casey, C. M., & Werf, P. v. d. 2020, *ApJ*, **889**, L11
- Sanders, R. L., et al. 2020, *MNRAS*, **491**, 1427
- Satyapal, S., Kamal, L., Cann, J. M., Secrest, N. J., & Abel, N. P. 2021, *ApJ*, **906**, 35
- Schöck, M., et al. 2009, *PASP*, **121**, 384
- Schreiber, C., et al. 2015, *A&A*, **575**, A74
- Scoville, N., et al. 2007, *ApjS*, **172**, 38
- Scoville, N., et al. 2017, *ApJ*, **837**, 150
- Senarath, M. R., et al. 2018, *ApJ*, **869**, L26
- Shull, J. M., & McKee, C. F. 1979, *ApJ*, **227**, 131
- Spinoglio, L., & Malkan, M. A. 1992, *ApJ*, **399**, 504
- Spinoglio, L., Malkan, M. A., Smith, H. A., González-Alfonso, E., & Fischer, J. 2005, *ApJ*, **623**, 123
- Spinoglio, L., et al. 2015, *ApJ*, **799**, 21
- Spinoglio, L., et al. 2017, *PASA*, **34**, e057
- Spinoglio, L., et al. 2021a, *PASA*, **38**, e021
- Spinoglio, L., et al. 2021b, arXiv e-prints, [arXiv:2111.04434](https://arxiv.org/abs/2111.04434)
- Stanway, E. R., & Eldridge, J. J. 2018, *MNRAS*, **479**, 75
- Steidel, C. C., et al. 2016, *ApJ*, **826**, 159
- Stern, J., & Laor, A. 2012, *MNRAS*, **426**, 2703
- Sturm, E., et al. 2002, *A&A*, **393**, 821
- Swinyard, B., et al. 2009, *ExA*, **23**, 193
- Tamura, Y., et al. 2019, *ApJ*, **874**, 27
- Tielens, A. G. G. M., & Hollenbach, D. 1985, *ApJ*, **291**, 722
- Tommasin, S., Spinoglio, L., Malkan, M. A., & Fazio, G. 2010, *ApJ*, **709**, 1257
- Tommasin, S., et al. 2008, *ApJ*, **676**, 836
- Troncoso, P., et al. 2014, *A&A*, **563**, A58
- Veilleux, S., et al. 2009, *ApjS*, **182**, 628
- Venemans, B. P., et al. 2020, *ApJ*, **904**, 130
- Vishwas, A., et al. 2018, *ApJ*, **856**, 174
- Walter, F., et al. 2018, *ApJ*, **869**, L22
- Wooten, A., & Thompson, A. R. 2009, *IEEE Proc.*, **97**, 1463
- Wright, G. S., et al. 2015, *PASP*, **127**, 595
- Zhuang, M.-Y., Ho, L. C., & Shangguan, J. 2019, *ApJ*, **873**, 103